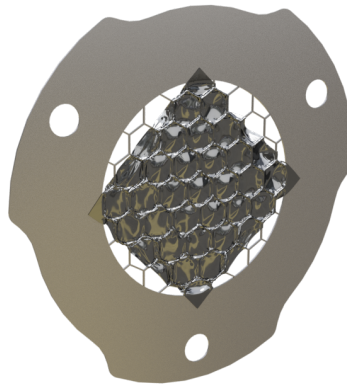


Development of an Intense Positron Beam lifetime spectrometer

M.G.M. Boekel

*Master Thesis Applied Physics
Reactor Institute Delft*

November 14, 2022



The cover image is a 3D render of a thin foil positron moderator.

Development of an Intense Positron Beam lifetime spectrometer

by

M.G.M. Boekel

In partial fulfillment of the requirements
for the degree of Master of Science in Applied Physics

at the Delft University of Technology.

To be defended at 11:00 on December 1st, 2022.

Supervisor: Dr. H. Schut
Thesis committee: Dr. W.G. Bouwman
Dr. S.W.H. Eijt
Co-supervisor: Ing. M.R. de Boer

Author: Mark G.M. Boekel
Student number: 4688023
Track: Physics for Instrumentation
Faculty: Reactor Institute Delft (RID)
Research Group: Neutron and Positron Methods for Materials (NPM2)
Date: November 14, 2022

Summary

A new intense positron beam lifetime spectrometer is being developed at the Reactor Institute Delft that should be able to perform positron lifetime measurements with depth profiling. The positrons are generated by pair formation using high energy gamma-photons from the Hoger Onderwijs Reactor. This new positron lifetime spectrometer has a unique way to determine the point in time when a positron is injected into the sample material. Before the positrons are injected, they travel through a carbon foil which will then release secondary electrons. These secondary electrons are detected by a microchannel plate detector which starts a timer. Once the positron annihilates within the sample it releases two 511 keV photons. If one of these photons is detected, the timer is stopped, and the elapsed time is stored. Many measurements of the elapsed time are needed to create a positron lifetime spectrum.

The main research goal is to further develop this new positron lifetime spectrometer such that it is able to measure a positron lifetime spectrum. Multiple adaptations and tests were performed in order to achieve the research goal.

At the start of the project, the positron lifetime spectrometer could not deliver a thermalized positron beam from its 50 nm thick tungsten moderator. This problem was solved by reannealing this moderator. Additionally, a new moderator was prepared and annealed. The Variable Energy Positron facility was used to perform characterization measurements on the moderators. This facility was modified to allow the transmission of positrons through the moderator and measure emitted thermalized positrons by the moderator. At the same time, a model based on the positron transport equation was developed to simulate and verify the characterization experiments. Both the old and new moderator have shown that they can emit thermalized positrons. The old moderator has a measured efficiency of 0.073 ± 0.002 when the positron implantation energy equals 3.7 ± 0.1 keV. The new moderator has a measured efficiency of 0.123 ± 0.002 when the positron implantation energy equals 3.2 ± 0.1 keV.

During the project, the microchannel plate detector which measures secondary electrons had to be tested, because no detections were observed in previous experiments. Additionally, the scintillation detector which is used to measure annihilation photons was tested. Eventually, both detectors have showed that they work correctly.

Finally, the positron beam of the lifetime spectrometer was aligned such that the positrons travel through the carbon foil onto the target. Secondary electrons generated by positrons have been measured by the microchannel plate detector. Afterwards, the first positron lifetime spectrum was measured using this new instrument. This lifetime spectrum is still rather crude as it shows multiple peaks and a time resolution function with a full width half maximum of 0.57 ns. The research goal of this project has been achieved, but further development is needed in order to accurately measure positron lifetimes.

Contents

Summary	4
1 Introduction	7
2 Theory	8
2.1 Positron annihilation	8
2.2 Behavior of positrons in solids	9
2.2.1 Positron interactions	9
2.2.2 Positron work function	11
2.2.3 Positronium	11
2.2.4 Positron implantation	12
2.2.5 Positron transport in solids	12
2.2.6 Model for thin foils	13
2.3 Detector theory	19
2.3.1 Scintillation detector	19
2.3.2 Micro Channel Plate detector	20
2.3.3 Semiconductor detector	20
2.4 Instrument theory	22
2.4.1 Positron Annihilation Lifetime Spectroscopy	22
2.4.2 Methods for positron production	24
2.4.3 Positron moderator	24
3 Instruments and Methods	25
3.1 Instruments	25
3.1.1 Intense Positron Beam lifetime spectrometer	25
3.1.2 Variable Energy Positron facility	28
3.2 Methods	31
3.2.1 Positron moderators	32
3.2.2 Moderator annealing	33
3.2.3 Moderator characterization method	33
3.2.4 Monoenergeticity and beam profile measurement of VEP facility	35
3.2.5 Detector testing	35
4 Results and Discussion	38
4.1 Instrument verification	38
4.1.1 Microchannel plate detector	38
4.1.2 Scintillation detector	39
4.1.3 Variable Energy Positron facility	39
4.2 Moderator characterization	43
4.2.1 Annealing of the moderators	43
4.2.2 Thin foil model simulation	45
4.2.3 Measurement of positron annihilation in the moderator	48
4.2.4 Measurement of positron transmission through the moderator	51
4.3 Intense Positron Beam lifetime spectrometer	56
4.3.1 Beam alignment	56
4.3.2 Positron lifetime spectrum measurement	58
5 Conclusion	61
Acknowledgements	62
Appendices	64
A Derivation of the Green's function of the positron transport equation	64

CONTENTS

B Moderator foil handling	69
C High temperature oven controller	70
D Full drawing of the VEP facility	72
E Python code for moderator simulation	73

1 Introduction

Positron Annihilation Lifetime Spectroscopy (PALS) is a unique method for identifying defects and their concentrations in materials [1]. Open volume defects form a potential well due to the missing atom cores from the crystal lattice. The positively charged positrons can be trapped by the open volume defects. Trapped positrons have an increased lifetime due to the lower electron density within defects [2]. This lifetime can be measured to obtain information about the type and concentration of defects in a solid material.

The positron lifetime can be measured by a relatively simple setup using a ^{22}Na source. This source emits positrons, but for every positron, a gamma-photon is generated as well at nearly the same point in time. The positrons that are emitted by the source are implanted into a solid sample. These implanted positrons eventually annihilate and will predominantly produce two characteristic gamma photons.

The photons from the source and from the annihilation are separately measured by two fast scintillation detectors. They are each configured to measure a specific energy. The first detector measures the decay photons of the ^{22}Na source and the second detector measures the annihilation radiation. Once both detectors measure photons with the correct energy, the difference in time is registered by a computer to obtain the lifetime of a single positron. At least 10^6 annihilation detections are needed to get a complete positron lifetime spectrum [2].

This simple PALS setup is compact and has a good time resolution, but does not support depth profiling and has a low count rate due to the need of small sized radioactive sources. Thin or multilayered samples cannot be studied without depth profiling. This problem can be solved if a PALS instrument is able to generate a monoenergetic positron beam with variable energy. The positron implantation profile is known and parameterized. Therefore, the measured positron lifetime versus the material depth can be resolved.

A new instrument is being developed at the Reactor Institute Delft (RID) that should be able to perform PALS measurements with depth profiling. Instead of using a radioactive positron source, this new instrument utilizes an intense beam of Positrons from the Hoger Onderwijs Reactor (POSH). This beam has an observed intensity of $0.7 \times 10^8 \text{ s}^{-1}$ in a 10 mm beam spot [3]. Additionally, the beam consists of slow positrons and can therefore be efficiently moderated.

This new intense positron beam lifetime spectrometer, which is called POSH-PALS, has a unique way to determine the point in time when a single positron is implanted into the sample. Before the positrons are implanted, they travel through a carbon foil which will then release secondary electrons. These secondary electrons are detected by a Microchannel Plate (MCP) detector. The annihilation photons are detected by a fast scintillation detector near the sample.

Other institutes have built PALS facilities that support depth profiling [4] [5]. These facilities generate positron bunches that arrive at sample at a known point in time. A fast scintillation detector is used as well to measure the annihilation radiation.

The main research goal is to further develop the POSH-PALS facility such that it is able to measure a positron lifetime spectrum. Once this has been achieved, the time resolution and the positron lifetime can be measured for the first time. These results will open the way for further improvement.

Multiple adaptations and tests have been performed before the instrument is able to function. The positron beam has been aligned and the detectors were tested. Furthermore, a new positron moderator has been annealed and installed.

To verify that the new positron moderator functions well, it was fully characterized by using the Variable Energy Positron (VEP) facility. This facility generates a narrow and monoenergetic positron beam that is used for positron spectroscopy. The characterization experiments include a measurement of the emitted thermalized positron fraction versus the implantation energy. All characterization results were verified and fitted with a newly developed model which is based on the positron transport equation. With this model, the characterization experiments can be simulated.

2 Theory

This chapter starts with an introduction about positron annihilation. This is followed by Section 2.2 which explains the behavior of positrons in solids and introduces a model for positrons in thin foils. In Section 2.3, the working principle of radiation detectors needed for positron spectroscopy is described. Finally in Section 2.4, positron annihilation lifetime spectroscopy is introduced together with other instrument theory.

2.1 Positron annihilation

The process in which a positron (e^+) and its antiparticle, the electron (e^-) are converted into photons is called annihilation [6]. In an annihilation event, one or more photons are produced. Positrons that are implanted into solids will mostly annihilate into two photons

$$e^- + e^+ \rightarrow \gamma_1 + \gamma_2. \quad (1)$$

The other annihilation modes, e.g., 3γ or 4γ annihilation, are rare and are therefore practically not important for spectroscopy using slow positrons implantation. Positrons with a kinetic energy of several tens of kiloelectronvolts or lower are defined as slow. Energy and momentum must be conserved in the process of annihilation. At rest, the positron electron pair will generate two photons with an energy of $m_0c^2 = 511$ keV each, where m_0 is the rest mass of the electron and c is the speed of light. These two photons travel in opposite direction relative to each other. When not at rest, the positron electron pair carry a net momentum denoted as vector \mathbf{p} . The momentum is transferred to the photons by a Doppler shift in energy ΔE_γ or an angular deviation $\Delta\theta_{\gamma-\gamma}$. This energy shift and angular deviation of the photons are proportionally dependent on the parallel momentum \mathbf{p}_\parallel and the perpendicular momentum \mathbf{p}_\perp , respectively. These two vectors are components of vector \mathbf{p} and are parallel or perpendicular to the traveling direction of one of the annihilation photons. All momentum vectors and annihilation photons are shown in Figure 1.

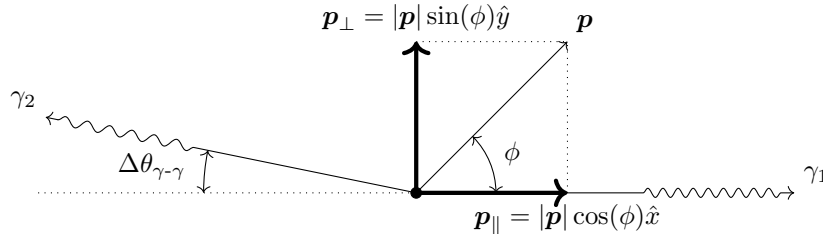


Figure 1: A vector diagram showing the net momentum \mathbf{p} of the positron electron pair and the emission of two annihilation photons. The net momentum consists of its parallel component p_\parallel and perpendicular component p_\perp . The emitted photons have an energy shift and an angular deviation $\Delta\theta_{\gamma-\gamma}$. This diagram shows an exaggerated angular deviation, which in reality is very small for positron annihilation in solids. Therefore, the annihilation photons will travel in nearly the opposite direction.

In practice, the momentum of a positron p_+ is much lower than the momentum of electrons p_- in solids right before the annihilation event, so

$$p_+ \ll p_- \rightarrow |\mathbf{p}| \approx p_-. \quad (2)$$

Therefore, it can be assumed that the energy shift and the angular deviation of the emitted photons only depends on the momentum of the electron. The probability of annihilation increases with lower positron energies. Therefore, most positrons within a solid will not annihilate before they are slowed down by inelastic scattering to thermal energies.

The electrons in ordinary solids have a kinetic energy that is much lower than the mass-energy equivalence of itself and the positron;

$$|\mathbf{p}|c \ll m_0c^2. \quad (3)$$

Consequently, the angle between the two photons will only deviate slightly from 180° . If all these assumptions hold, then the energy shift of the photons is given by:

$$\Delta E_\gamma = \frac{p_{\parallel} c}{2}. \quad (4)$$

The photon that travels in the same direction as the parallel momentum will have an energy of $m_0 c^2 + \Delta E_\gamma$. The other photon will have a lower energy of $m_0 c^2 - \Delta E_\gamma$. The angular deviation between the photons is given by:

$$\Delta\theta_{\gamma-\gamma} = \frac{p_{\perp}}{m_0 c}. \quad (5)$$

Measuring the energy shift or angular deviation of the emitted gamma photons, gives information about the momentum of the electrons within the solid. The positron lifetime τ is in the classical limit a function of the local electron density n_e and is described by:

$$\frac{1}{\tau} = \lambda_0(n_e) = \pi r_0^2 c n_e, \quad (6)$$

where λ_0 is the positron annihilation rate and r_0 is the classical electron radius [7].

2.2 Behavior of positrons in solids

This section will discuss the behavior of slow and monoenergetic positrons that are injected into (thin) solids. For thin enough foils, transmission of slow positrons is possible. The illustration in Figure 2 shows a simplified setup where a monoenergetic positron beam is injected into a thin solid.

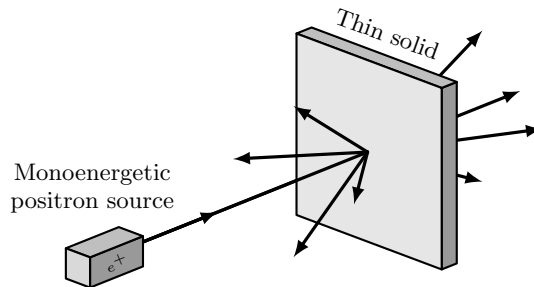


Figure 2: A simplified drawing of a source which injects monoenergetic positrons into a thin solid. Positrons interact within the solid. These positrons can annihilate or escape the foil. Other positrons can form positronium.

2.2.1 Positron interactions

A slow positron that hits the surface of a solid can undergo several types of interactions. Some incident positrons will be backscattered elastically, and form diffracted beams [6]. The other positrons enter the solid and start slowing down. These positrons will transfer most of their kinetic energy to inelastic electron scattering and phonon production [6]. The positrons keep slowing down until their kinetic energy is equalized to the thermal energy of the solid. Therefore, the slowing down process to thermal energies is called thermalization.

Positrons can scatter out of the solid. Then, they are emitted as free positrons or as positronium (Ps). This can happen for thermalized and non-thermalized positrons. These non-thermalized positrons are also known as epithermal positrons. The thermalized positrons that reach the surface of the solid can have the extra possibility to be trapped by the surface potential. These are surface bound positrons. In the case of thin foils, surface trapping and the emission of positrons and positronium can also occur on the other side of the foil. If the foil is too thick, then the positrons will not be able reach the other surface before annihilation.

Positrons have always the possibility to annihilate with an electron inside the solid, but this probability increases with lower positron energies. As a result, most positrons will be thermalized before they annihilate.

In Figure 3, a drawing is shown that displays the interactions that can occur as a result of a positron beam that is incident on a solid.

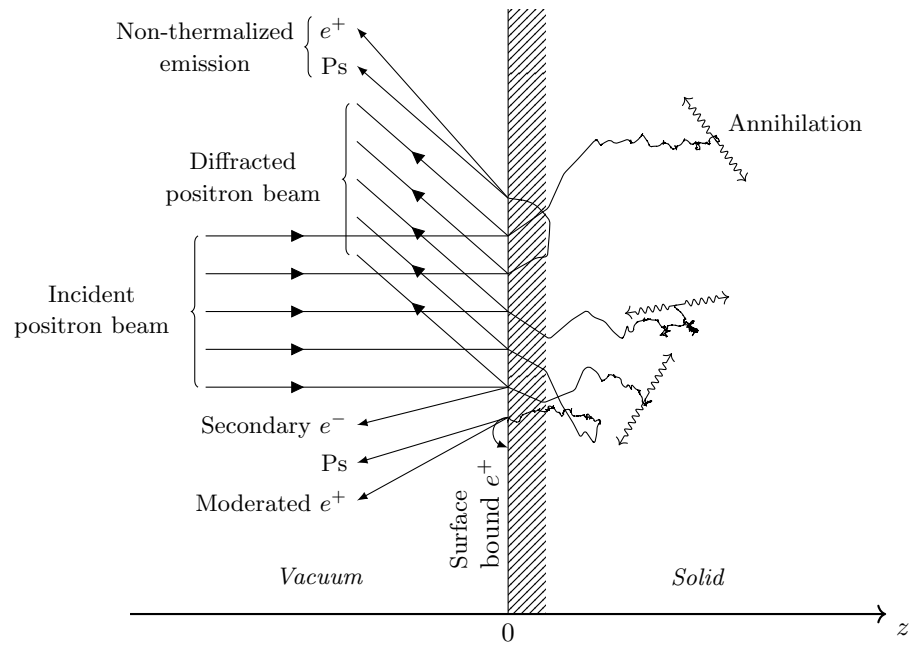


Figure 3: The interactions that occur as a result of a slow positron beam hitting a solid. (This drawing is mostly based on a figure that is shown in [8])

2.2.2 Positron work function

The positron work function ϕ_+ is defined as the minimum energy required to remove a positron from a solid to just outside the surface in vacuum, which can be expressed by:

$$\phi_+ = -E_0 - E_c - D \quad (7)$$

[6]. In this equation, E_0 represents the repulsive interaction of the positrons with the ion cores, D is the surface dipole barrier and E_c is the potential caused by the interactions between the positron and the cloud of electrons. A drawing of all potentials at the surface of a metal is shown in Figure 4.

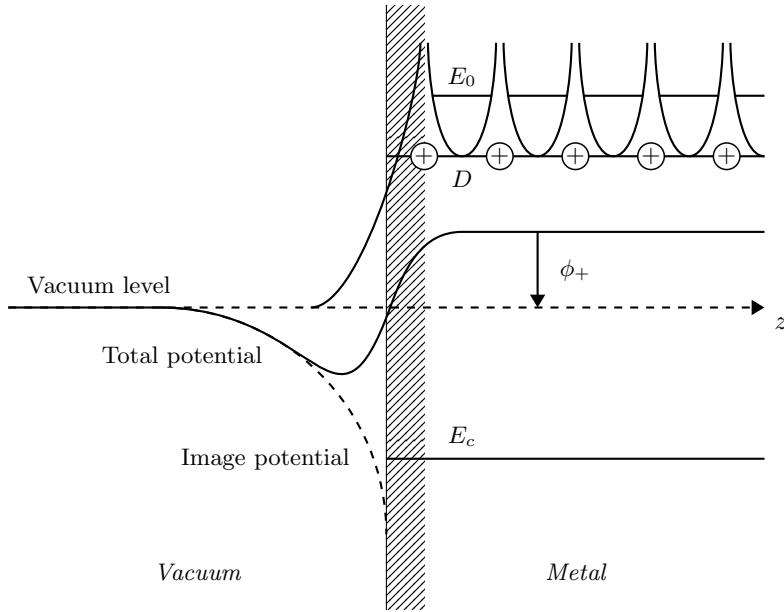


Figure 4: The total potential for positrons at the surface of a solid metal. The positron work function ϕ_+ , is a combination of the bulk chemical potential and the surface dipole barrier D . The positron chemical potential includes terms due to correlation with the conduction electrons (E_c) and a repulsive interaction of positrons with the ion cores (E_0). [9] In the case of this figure, the metal has a negative ϕ_+ . (This drawing is mostly based on a figure that is shown in [9])

Solids with a negative ϕ_+ have the ability to emit thermalized positrons. The energy of these emitted positrons is equal to ϕ_+ plus their thermal energy.

2.2.3 Positronium

Positrons and electrons can together form a bound state that is called positronium (Ps). For most materials (such as metals) the formation of positronium only takes place at the surface. There are two known ground states: para-positronium (p-Ps) with a lifetime in vacuum of 125 ps, and ortho-positronium (o-Ps) with a lifetime in vacuum of 142 ns [6]. Once p-Ps decays, it mostly releases two 511 keV photons. The decay process of o-Ps mainly emits three photons with a combined energy of 1022 keV. When a positronium atom is formed, it has a fixed probability of 1/4 to become p-Ps. Otherwise it becomes o-Ps.

2.2.4 Positron implantation

A monoenergetic positron injected into a solid is slowed down until it is thermalized. While a positron slows down, it travels some distance within the solid. The net travel distance from the surface is called the implantation depth. This distance follows a specific probability distribution that is called an implantation profile. Once the implantation profile is known, then it is possible to resolve depth information with a variable energy positron beam.

It is assumed that the relation between the mean implantation depth \bar{z} and positron energy E is governed by a power law,

$$\bar{z} = AE^n, \quad (8)$$

which was originally developed for electron stopping [9]. In this expression, A is a material dependent property and n is a constant. Mills and Wilson [10] have verified Equation 8 experimentally. Later, Valkealahti [11] investigated positron and electron implantation using Monte-Carlo simulations. These simulations showed implantation profiles that can be parameterized by a Makhov distribution;

$$P(z, E) = \frac{mz^{m-1}}{z_p^m} \exp \left[- \left(\frac{z}{z_p} \right)^m \right], \quad (9)$$

where:

$P(z, E)$	Energy dependent positron implantation density	(nm ⁻¹),
m	Shape parameter	(-),
E	Positron implantation energy	(keV),
$z_p(E)$	Penetration parameter	(nm).

Vehanen [12] reports that the shape parameter has the value of $m = 2.0 \pm 0.1$, and that the penetration parameter can be expressed as:

$$z_p = \frac{\alpha E^n}{\rho \Gamma \left(\frac{m+1}{m} \right)} = \frac{\bar{z}}{\Gamma \left(\frac{m+1}{m} \right)}. \quad (10)$$

Here, the values of n and α are reported to be 1.62 ± 0.05 and $(4.0 \pm 0.3) \mu\text{g} \cdot \text{cm}^{-2} \cdot \text{keV}^{-1.62}$ respectively [12]. Furthermore, this expression depends on ρ , the mass density of the solid in $\mu\text{g} \cdot \text{cm}^{-3}$.

2.2.5 Positron transport in solids

Once positrons are implanted into a solid, they show diffusive behavior. This is mainly governed by Coulomb interactions between the positron and the electrons and ion cores [6]. If there is an electric field inside the solid, then the positrons will drift in the direction of that electric field. The positrons keep moving by diffusion and drifting through the solid until they annihilate or escape it.

The one-dimensional steady-state transport of thermalized positrons with annihilation is described by:

$$\underbrace{D_+ \frac{d^2 c(z)}{dz^2}}_{\text{Diffusion}} - \underbrace{\frac{d(v_d(z)c(z))}{dz}}_{\text{Electric field}} - \underbrace{(\nu_t n_t(z) + \lambda_b)c(z)}_{\text{Annihilation}} + \underbrace{I(z, E)}_{\text{Implantation}} = 0 \quad (11)$$

[6], where:

D_+	Positron diffusion coefficient	(nm ² · s ⁻¹),
$c(z, E)$	Steady-state thermalized positron concentration	(nm ⁻¹),
$v_d = \mu E(z)$	Positron drift velocity	(nm · s ⁻¹)
μ	Positron mobility	(nm ² · V ⁻¹ · s ⁻¹),
$E(z)$	Electric field strength	(V · nm ⁻¹),
ν_t	Specific positron trapping rate for defects	(s ⁻¹),
$n_t(z)$	Defect fraction	(-),
λ_b	Bulk annihilation rate	(s ⁻¹),
$I(z, E)$	Energy dependent positron implantation density rate	(nm ⁻¹ · s ⁻¹).

The solution of this equation gives the steady state positron distribution. With Fick's law, this will give the diffusive positron flux:

$$J(z) = -D_+ \frac{dc(z, E)}{dz}. \quad (12)$$

The relation between effective diffusion length L_+ and the diffusion constant is given by:

$$L_+ = \sqrt{\frac{D_+}{\lambda_b + n_t \nu_t}}. \quad (13)$$

The diffusion length for a defect free bulk material is given by:

$$L_{b+} = \sqrt{\frac{D_+}{\lambda_b}} = \sqrt{D_+ \tau_b}, \quad (14)$$

where τ_b is the positron lifetime in the bulk material.

2.2.6 Model for thin foils

In this section, a model for thin foils in a monoenergetic positron beam is introduced. A foil is considered thin if slow positrons are able to be transmitted through the foil. The purpose of the model is to determine the efficiency of positron moderators by fitting measurement data of variable energy positron experiments. For example, the energy dependent positron transmission curve, gives useful information about the diffusion length L_+ and the thickness L of the foil.

This model is developed to reassemble an ideal variable energy positron experiment with two detectors. One detector measures all the annihilation photons that are generated in or near the foil. The other detector measures the positrons that are transmitted through the foil. An applied magnetic field \mathbf{B} that is parallel to the z -axis, forces all transmitted positrons into the transmission detector. This ideal experimental setup is shown in Figure 5.

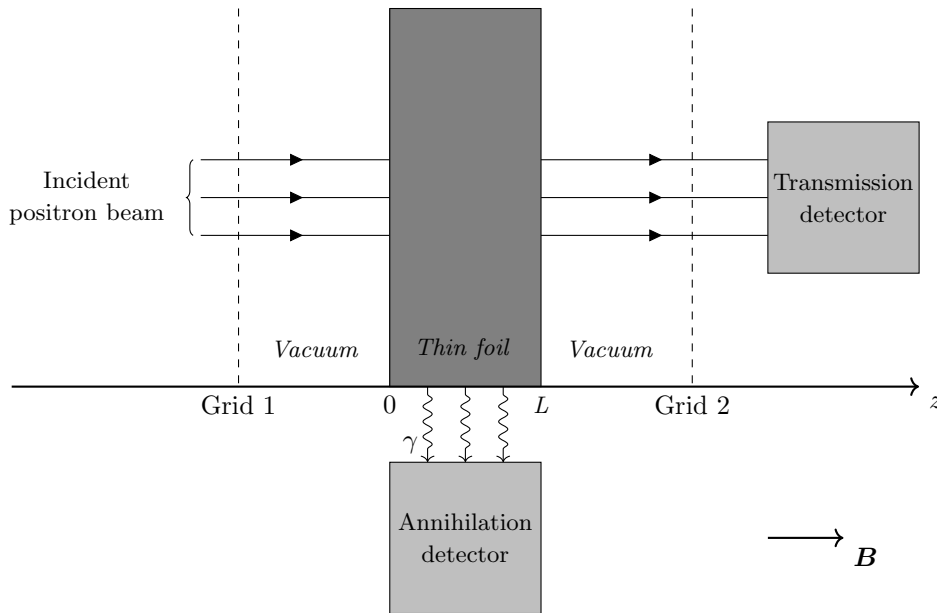


Figure 5: An illustration of the thin foil model. A monoenergetic positron beam is incident on the foil. This foil is placed between two retarding field grids. A voltage can be set on these grids to repel thermalized positrons back into the foil. In this model, a magnetic field is applied in the z -direction for guiding the positrons. The annihilation detector measures positron annihilation from in or near the sample by detecting characteristic 511 keV γ -photons. The transmission detector measures all positrons that emerge from the rear side of the foil.

Positron implantation model

The implantation curve for positrons injected into a solid is parameterized by the Makhov distribution. For an infinite thick material, the integral of this distribution equals 1. In this model, the Makhov

distribution is truncated by integrating it from 0 to thickness L . Then, a part of the positrons will be implanted into the foil and the other part will be transmitted.

Incident positrons have, next to implantation and transmission, the possibility to backscatter as epithermal positrons. The fraction of backscattered epithermal positrons $F_{be\pi}$ increases with lower positron energies. This fraction can be determined by a method that is suggested by Britton [13]:

$$F_{e\pi}(E) = \int_0^\infty P(z, E) \exp\left(\frac{-z}{l_{e\pi}}\right) dz, \quad (15)$$

where $l_{e\pi}$ is the epithermal scattering length. This holds for an infinitely thick material. For a thin foil, the positrons that are transmitted end up in vacuum where they cannot scatter anymore. Therefore, it is assumed that the improper integral can be changed to an integral from 0 to L :

$$F_{be\pi}(E) = \int_0^L P(z, E) \exp\left(\frac{-z}{l_{e\pi}}\right) dz. \quad (16)$$

Also, it is assumed that the same process of epithermal positron emission occurs on the back side of the foil. The probability density for positron implantation with epithermal scattering would then be:

$$D_i(z, E) = \begin{cases} P(z, E) \left[1 - \exp\left(\frac{-z}{l_{e\pi}}\right) - \exp\left(\frac{z-L}{l_{e\pi}}\right)\right] & \text{for } 0 \leq z \leq L \\ 0 & \text{otherwise} \end{cases} \quad (17)$$

The fraction of transmitted epithermal positrons $F_{te\pi}$ is determined by:

$$F_{te\pi}(E) = \int_0^L P(z, E) \exp\left(\frac{z-L}{l_{e\pi}}\right) dz. \quad (18)$$

The fraction of implanted positrons into the foil can be found by integrating $D_i(z, E)$:

$$F_i(E) = \int_0^L D(z, E) dz. \quad (19)$$

To visualize both probability densities $P(z, E)$ and $D_i(z, E)$ and the implanted positron fraction, a plot is shown in Figure 6.

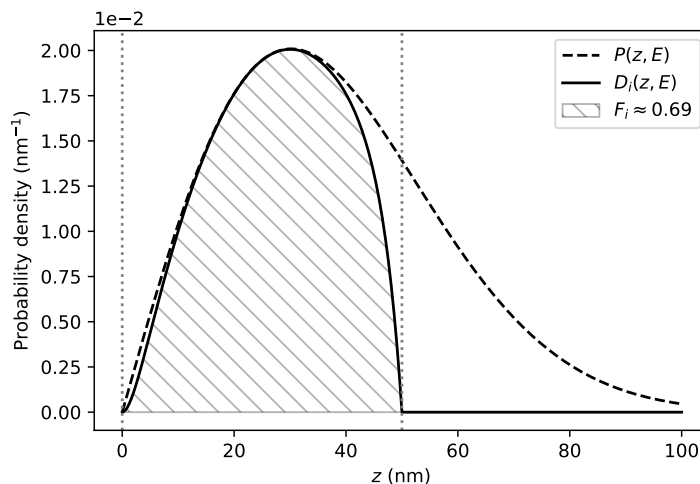


Figure 6: The energy dependent probability density for positron implantation. This plot shows the Makhov distribution $P(z, E)$. The other curve is a truncated Makhov distribution combined with the effect of epithermal positron emission. This curve is the probability density for thin foils $D_i(z, E)$. Both curves are calculated for tungsten with a positron beam energy of 6 keV. For $D_i(z, E)$, the foil has a thickness of 50 nm and an epithermal scattering length of $l_{e\pi} = 3$ nm. The thickness of the foil is indicated by the vertical dotted lines. The surface below $D_i(z, E)$ is filled to show the fraction of implanted positrons F_i .

For solving the positron transport equation, the energy dependent positron implantation density rate $I(z, E)$ must be known. $I(z, E)$ can simply be found by multiplying the implantation probability density with the incident positron rate R :

$$I(z, E) = RD_i(z, E). \quad (20)$$

The incident positron rate uses the unit: s^{-1} . The physical quantity R is only needed for calculating the exact number of positrons, but for positron fractions, it cancels out.

Positron transport in a thin foil

The steady state positron diffusion equation shown in Equation 11 requires simplifications to be solved analytically. In this model for thin foils, it is assumed that the foil is composed of a homogeneous and electrically conductive material. Therefore, the defect concentration n_t is constant. An electrically conductive material would allow to assume that there is no internal electric. Consequently, the drift velocity is zero:

$$v_d = \mu E(z) = 0, \quad (21)$$

thus, eliminating the electric field term of Equation 11. These assumptions reduce the problem into an inhomogeneous Helmholtz equation:

$$D_+ \frac{d^2 c(z)}{dz^2} - (\nu_t n_t + \lambda_b) c(z) + I(z) = 0. \quad (22)$$

In this model, the thin foil occupies the space where $0 \leq z \leq L$ and the complete xy -plane.

The space where $z < 0$ or $z > L$ is a vacuum where positrons move ballistically. Therefore, positrons do not return to the foil once they escaped it. This will result in the positron concentration being zero at the surface of foil and so, the boundary conditions are defined as:

$$c(0, E) = c(L, E) = 0. \quad (23)$$

Now, with the simplifications and boundary conditions, the Green's function for $c(z, E)$ can be solved analytically and equals:

$$G(z; z_0) = \begin{cases} \frac{-\sinh(\alpha(z_0-L)) \sinh(\alpha z)}{\beta \sinh(\alpha L)} & \text{for } z < z_0 \\ \frac{-\sinh(\alpha(z-L)) \sinh(\alpha z_0)}{\beta \sinh(\alpha L)} & \text{for } z > z_0 \end{cases}, \quad (24)$$

where,

$$\alpha = \sqrt{\frac{\nu_t n_t + \lambda_b}{D_+}}, \quad \beta = \sqrt{D_+(\nu_t n_t + \lambda_b)}. \quad (25)$$

The same solution for the Green's function of $c(z, E)$, but with another equation can be found with the eigenfunction expansion method and results in:

$$G(z; z_0) = \sum_{n=1}^{\infty} \frac{2 \sin\left(\frac{\pi n z_0}{L}\right) \sin\left(\frac{\pi n z}{L}\right)}{L \left(\frac{\pi^2 n^2}{L^2} D_+ + \nu_t n_t + \lambda_b\right)}. \quad (26)$$

A plot of the Green's function of $c(z, E)$ is shown in Figure 7.

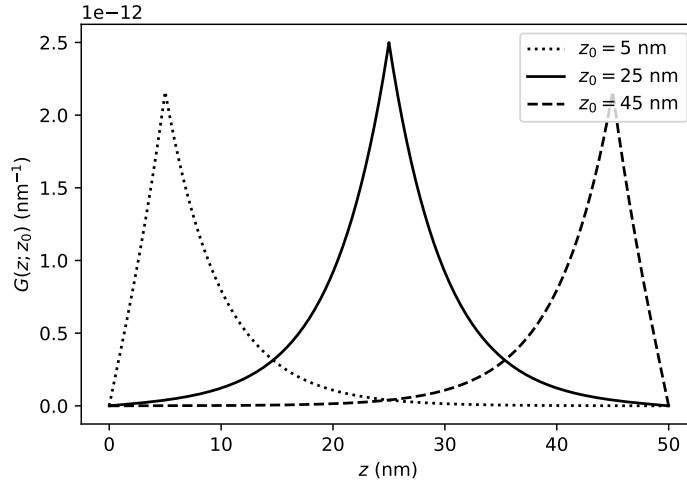


Figure 7: The Green's function of $c(z, E)$. For this example, the functions are plotted for $z_0 = 5, 25$ and 45 nm. The thickness L equals 50 nm and the diffusion length L_+ is set on 5 nm.

The derivation both Green's functions of $c(z, E)$ with additional plots are included in Appendix A.

With the Green's function and the energy dependent positron implantation rate $I(z, E)$, the steady-state thermalized positron concentration can be given by:

$$c(z, E) = \int_0^L I(z_0, E)G(z; z_0)dz_0. \quad (27)$$

Positron fractions and surface branching

In this model, a number of processes will decide the fate of all positrons. The incident beam of positrons delivers the total positron fraction. This fraction equals 1. According to the implantation probability density described in Equation 17, there are epithermal positrons fractions that are backscattered (F_{bepi}) and transmitted (F_{tepi}). Also, there is a probability that positrons are just transmitted through the foil. This is the transmitted positron fraction:

$$F_{tr}(E) = \int_L^\infty P(z, E)dz = \exp \left[- \left(\frac{L}{z_p} \right)^m \right]. \quad (28)$$

The implanted positron fraction F_i indicates all positrons that are thermalized inside the foil and is given by Equation 19. These thermalized positrons can annihilate in the bulk material or in a trapped state. This gives the bulk annihilated fraction F_b and the trapped annihilated fraction F_t . These values are given by:

$$F_b(E) = \frac{\lambda_b}{R} \int_0^L c(z, E)dz, \quad (29)$$

$$F_t(E) = \frac{n_t \nu_t}{R} \int_0^L c(z, E)dz. \quad (30)$$

Not all thermalized positrons annihilate within the foil. These positrons will diffuse to the front or rear surface of the foil. With Fick's law from Equation 12, the fraction of positrons that diffuse to the front surface of the foil can be expressed with:

$$F_{fs}(E) = \frac{-D_+}{R} \left. \frac{dc(z, E)}{dz} \right|_{z=0}. \quad (31)$$

The same method can be used for the fraction of positrons that diffuse to the rear surface of the foil:

$$F_{rs}(E) = \frac{-D_+}{R} \left. \frac{dc(z, E)}{dz} \right|_{z=L}. \quad (32)$$

Once the positrons arrive at the surface of foil, they can end up being emitted as either a single positron or as positronium. Otherwise, the positrons are trapped into the surface potential of the foil. The probability for a positron to end up in each of these three states is a property of the surface of the foil. These probabilities are called branching ratios and are denoted by the symbol ϵ . In Table 1, all surface branching fractions for the thin foil model are shown.

Table 1: Surface branching fractions for both the front and the rear surface of the thin foil model.

Front surface		Rear surface
$F_{fe^+}(E) = \epsilon_{fe^+} F_{fs}(E)$	Positron emission fraction	$F_{re^+}(E) = \epsilon_{re^+} F_{rs}(E)$
$F_{fsb}(E) = \epsilon_{fsb} F_{fs}(E)$	Surface bound positron fraction	$F_{rsb}(E) = \epsilon_{rsb} F_{rs}(E)$
$F_{fpPs}(E) = 1/4 \epsilon_{fPs} F_{fs}(E)$	Para-positronium emission fraction	$F_{rpPs}(E) = 1/4 \epsilon_{rPs} F_{rs}(E)$
$F_{foPs}(E) = 3/4 \epsilon_{fPs} F_{fs}(E)$	Ortho-positronium emission fraction	$F_{roPs}(E) = 3/4 \epsilon_{rPs} F_{rs}(E)$

The total probability for all surface branching processes must be equal to 1:

$$\epsilon_{fe^+} + \epsilon_{fsb} + \epsilon_{fPs} = \epsilon_{re^+} + \epsilon_{rsb} + \epsilon_{rPs} = 1. \quad (33)$$

In Figure 8, a diagram is shown that visualizes all positron fractions in the thin foil model.

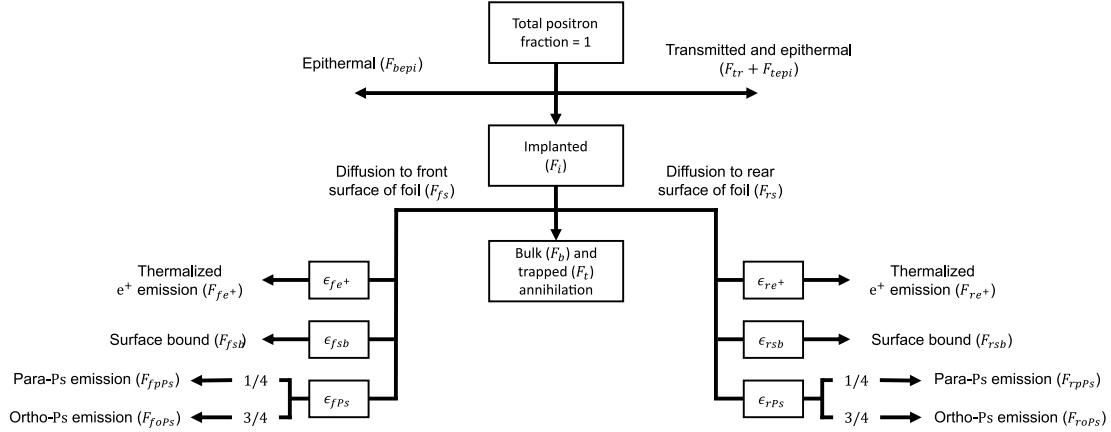


Figure 8: A diagram containing all positron fractions that are included in the thin foil model.

Measurement simulation

The virtual detectors that are shown in Figure 5 can give give useful information for what to expect in a real variable energy positron experiment. Also, fitting the model to measured data can give information about the properties of the foil.

Thermalized positrons that are emitted from the foil, can be reflected by the two low voltage grids. The grid in front of the foil is the primary grid G_1 and the one behind the foil is the secondary grid G_2 . The grids can have a positive charge (+) charge, which reflects the emitted thermalized positrons. A negative charged (-) grid allows the emitted thermalized positrons to escape from the thin foil. The normalized count rate that is measured by the virtual annihilation detector for negatively charged grids, is given by:

$$\frac{R_A}{R} = F_b + F_t + F_{fsb} + F_{rsb} + F_{fppPs} + F_{rppPs} \text{ for } G_1^-, G_2^-, \quad (34)$$

where R_A is the count rate of the virtual annihilation detector. The normalized count rate measured by the virtual transmission detector equals:

$$\frac{R_T}{R} = F_{tr} + F_{tepi} + \begin{cases} F_{re^+} & G_1^-, G_2^- \\ 0 & G_1^-, G_2^+ \end{cases}. \quad (35)$$

Here, R_T is the count rate of the virtual transmission detector. The normalized count rates for the other grid modes can be approximated by:

$$\frac{R_a}{R} \approx F_b + F_t + F_{fsb} + F_{rsb} + F_{fpPs} + F_{rpPs} + \begin{cases} F_{fe+} & \text{for } G_1+, G_2- \\ F_{re+} & \text{for } G_1-, G_2+ . \\ F_{fe+} + F_{re+} & \text{for } G_1+, G_2+ \end{cases} \quad (36)$$

The normalized count rate of the virtual transmission detector for $G_1 = +$, can be approximated by Equation 35. Both approximations assume that all the reflected thermalized positrons by G_1 and G_2 will annihilate inside or near the foil.

2.3 Detector theory

This section describes the functioning of a scintillation detector, a microchannel plate detector and a semiconductor detector.

2.3.1 Scintillation detector

A scintillation detector is a device that is able to detect gamma photons. This type of detector is useful for detecting 511 keV annihilation photons. The detector is composed out of two main components: the scintillation crystal and the photomultiplier tube. A scintillation crystal converts gamma photons into new lower energy photons. This process starts with a gamma photon that is absorbed by an atom of the crystal. This releases an energetic electron that is able to excite other atoms of the crystal. When these atoms return to their ground state, they each release a photon. These photons can be detected by the photomultiplier tube. Generally, sodium iodide crystals are used as scintillator material. For PALS measurements, barium fluoride crystals can be used for their fast response that is needed to achieve a good time resolution. There are also plastic scintillators available with faster response times.

Inside the photo multiplier tube, there is a photocathode, a focusing electrode, a detector plate and there are multiple dynodes. The photocathode converts photons from the scintillation crystal into electrons by the photoelectric effect. These electrons pass through a focusing electrode and are attracted by the charged dynodes. If the electron hits the first dynode, then the impact will release multiple secondary electrons. A number of dynodes are cascaded to further multiply the number of electrons. The last dynode will release the most secondary electrons. These electrons are caught by a detector plate which is connected to the counting electronics.

A simplified sectional view of a scintillation detector is shown in Figure 9.

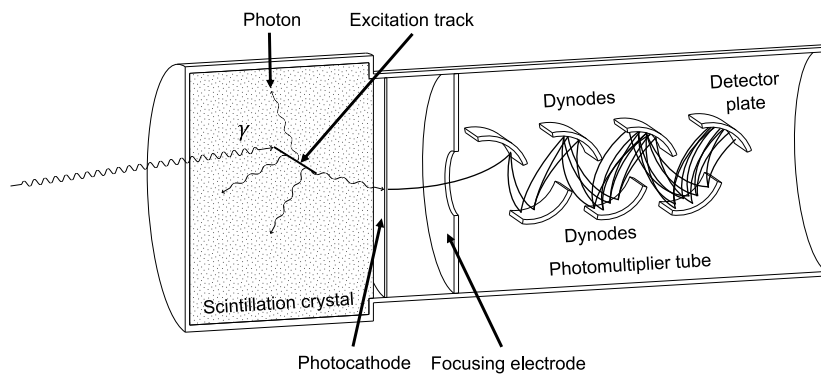


Figure 9: A simplified drawing of the sectional view of a scintillation detector. This detector is a combination of a scintillation crystal (left) and a photomultiplier tube (right). An incoming γ -photon is absorbed into the scintillation crystal. This process releases an electron that excites other atoms on its excitation track. The excited atoms release their energy in the form of a photon. The photocathode releases electrons inside the photomultiplier tube once it is hit by a photon. These electrons are attracted by the dynodes and multiplied. The electron multiplication factor per dynode is greater in reality than shown in this drawing. The detector plate is connected to counting electronics.

The full detector is completely sealed to block off light from outside. Around the scintillation crystal, there is a reflective layer to improve photon yield. The photomultiplier sits in a glass vacuum tube.

The dynodes of the photomultiplier are connected in series with resistors between them. Therefore, only a single high voltage power supply is needed to power the scintillation detector.

2.3.2 Micro Channel Plate detector

A Microchannel Plate (MCP) is a continuous dynode electron multiplier. The continuous dynode is shaped as a straight tube. A MCP detector is useful for detecting charged particles like positrons and electrons in a high vacuum. The MCP consists of a non-conducting plate which perforated with many tube dynodes. Each tube is coated from the inside with an electrical resistive material. Applying a voltage at both ends of each tube, results in an electric field inside it.

When a positron or electron hits the inside wall of the tube, it releases secondary electrons from the dynode just like in a photo multiplier tube. These secondary electrons are accelerated by the electric field and can also release other secondary electrons. At the other end of the tube, the secondary electrons escape the MCP. These secondary electrons are caught by a detector plate. Otherwise, a fluorescent screen could be added instead of a detector plate. This is useful for beam alignment, because the position of the beam in 2D space can then be resolved. The process of detecting a positron with a MCP detector is shown in Figure 10.

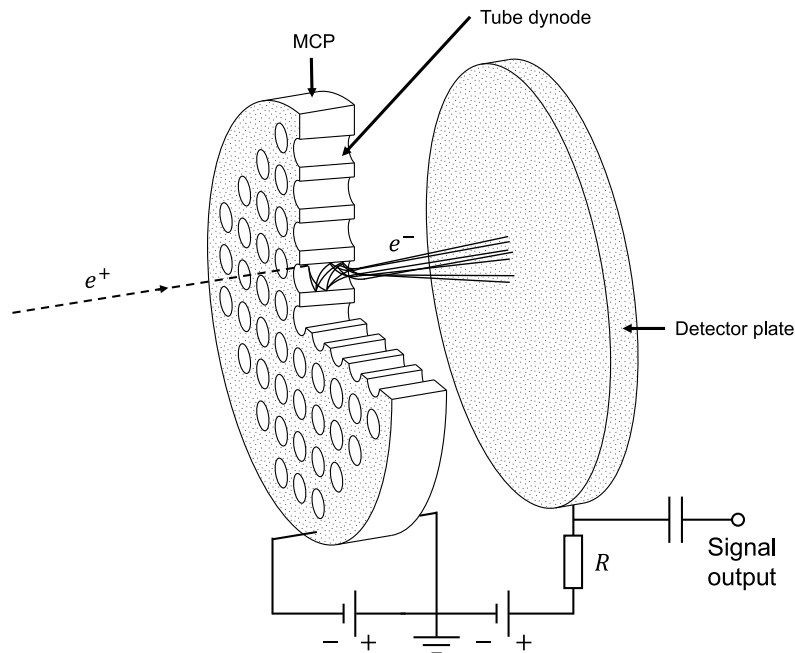


Figure 10: A simplified drawing of a MCP detector with oversized tube dynodes. An incoming positron hits a dynode of the Microchannel Plate (MCP). This is the disk on the left with holes in it. A quarter of the disk is cut out to give view of the inside of the tube dynodes. The impact of the positron releases secondary electrons. A voltage is applied on both ends of the tubes. This creates an electric field within the tubes. The secondary electrons are accelerated to the right and can generate other secondary electrons if they collide with the dynode. The electrons escape out of the MCP and hit the detector plate which is the disk on the right. Other MCP models have a fluorescent screen instead of a detector plate.

To increase the electron multiplying gain, the voltage can be increased or multiple MCPs can be stacked on top of each other.

The detector plate can be charged for attracting electrons. It is connected with a resistor and a capacitor. The capacitor isolates the high voltage of the detector plate from the counting electronics, but it passes the fast pulses.

2.3.3 Semiconductor detector

A semiconductor detector is a device that is able to detect gamma photons. These devices have a high energy resolution and for that reason have applications in positron Doppler broadening spectroscopy. The detector consists of a single crystal semiconductor between two electrodes. A voltage is applied to the electrodes to create an electric field within the crystal. Once a gamma photon is absorbed within the semiconductor crystal, it excites electrons above the band gap. This creates electron-hole pairs that drift

away from each other by the electric field. The drifting of electrons and holes is a temporary increase in electric current that can be electronically detected. In Figure 11, a planar semiconductor detector is shown where electron-hole pairs are created by the absorption of a gamma photon.

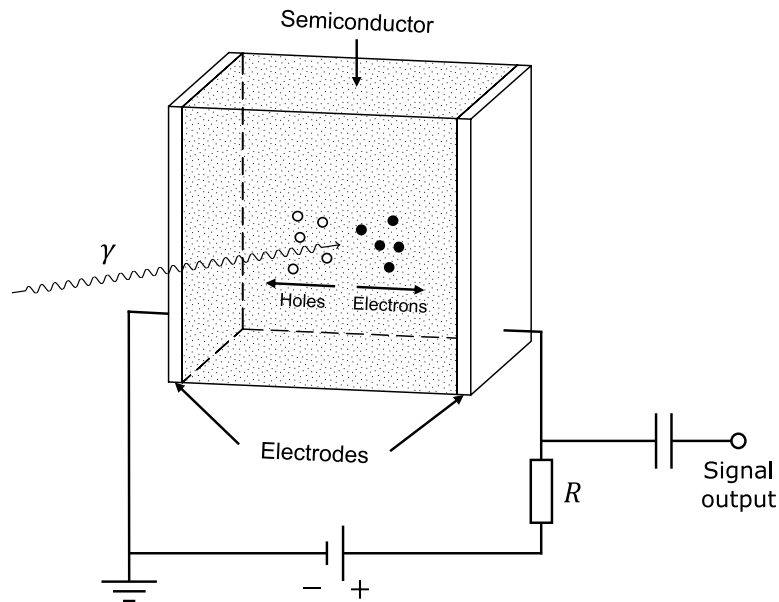


Figure 11: A simplified drawing of a planar semiconductor detector. A gamma photon is absorbed by the semiconductor material. Electron-hole pairs are then created which generate a detectable electric current.

A semiconductor detector can also be made with a coaxial geometry.

A typical semiconductor material is High Purity Germanium (HPGe). If the crystal is not ultra-pure, then the material can trap electrons and holes, which renders the detector useless for gamma or positron spectroscopy. HPGe detectors are cooled cryogenically to prevent electrons crossing the band gap by thermal energy. The detectors are usually cooled with liquid nitrogen or a cryogenerator.

2.4 Instrument theory

This section describes the basic theory of Positron Annihilation Lifetime Spectroscopy and shortly explains how positrons are artificially produced and moderated.

2.4.1 Positron Annihilation Lifetime Spectroscopy

Positron Annihilation Lifetime Spectroscopy (PALS) is a technique that measures the lifetime of positrons implanted into a solid sample material. For measuring the lifetime of a positron, the point in time when the positron enters the sample material and the point in time when the positron annihilates must be detected.

Open volume defects in materials have a lower electron density due to the missing atoms. This gives the positron a longer lifetime within open volume defects, because the annihilation probability is lower. As is shown in Equation 6, the positron lifetime τ is a function of the local electron density n_e . The missing atom core gives the open volume defect a lower potential than the surrounding volume, causing thermalized positrons to be trapped by them. These mechanisms make PALS a method to detect material defects with a high sensitivity. In Figure 12, the potential of a defect within a crystal lattice is shown.

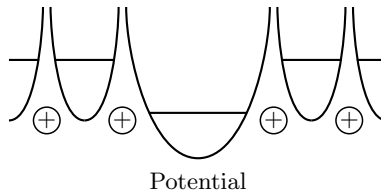


Figure 12: The potential of a defect within a crystal lattice. (This drawing is mostly based on a figure that is shown in [9])

The simplest PALS setup is to mount a ^{22}Na source close to sample. Therefore, the source needs to be small and flat. It is usually put in between two equal samples to minimize the escape of positrons. Two fast scintillation detectors will be used to measure two specific photon energies. One detector will capture the 'start' signal. This is a characteristic 1274 keV photon that is emitted from the ^{22}Na source after the positron is generated. The 'stop' signal is given if the other detector measures a characteristic 511 keV annihilation photon. The difference in time between the 'start' and 'stop' signal is measured, and this time is put into a histogram. This histogram called the positron lifetime spectrum, shows the number counts versus the measured positron lifetime. At least 10^6 annihilation detections are needed to get a complete lifetime spectrum [2].

The positron lifetime spectrum is modeled as a sum of exponential decay functions for all individual lifetime constants τ_i within the measured sample:

$$D(t) = \begin{cases} \sum_i I_i \exp\left(-\frac{t-t_s}{\tau_i}\right) & \text{for } t_s \leq t \\ 0 & \text{otherwise} \end{cases} \quad (37)$$

Here, I_i is the intensity of each lifetime component, t is the time and t_s is the point in time when a positron is injected into the sample material. In this spectrum, a time dependent behavior can be seen that is similar as the decay of radionuclides.

An experimentally obtained lifetime spectrum is different from the analytical description shown in Equation 37. Each PALS instrument has its own time resolution function f_σ that convolves with the lifetime spectrum. The time resolution function can be approximated by a single or a summation of multiple Gaussians. The simplest approximation is the use of a single Gaussian function:

$$f_\sigma(t) = \frac{1}{\sigma_t \sqrt{2\pi}} \exp\left(\frac{-t^2}{2\sigma_t^2}\right). \quad (38)$$

Now, the lifetime spectrum of an experimental setup $T(t)$ can be approximated by the following convolution:

$$T(t) = f_\sigma(t) * D(t) + I_b. \quad (39)$$

This equation includes the background intensity I_b . An example lifetime spectrum according to Equation 39 for two arbitrary time constants of $\tau_1 = 200$ ps and $\tau_2 = 1000$ ps is shown in Figure 13.

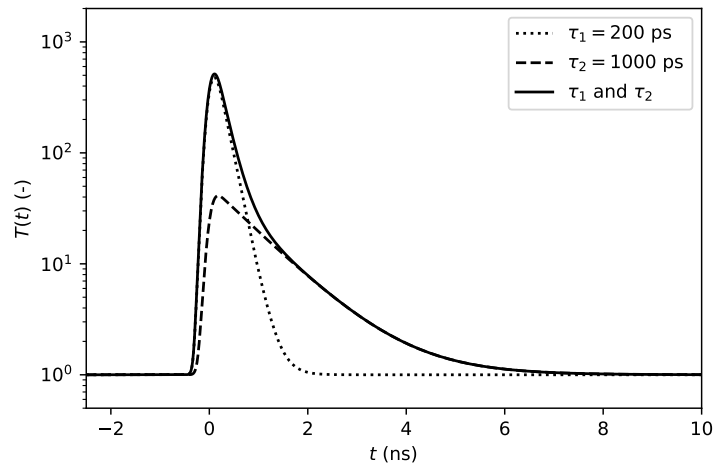


Figure 13: The expected positron lifetime spectrum according to Equation 39 for time constants $\tau_1 = 200$ ps and $\tau_2 = 1000$ ps with intensities $I_1 = 1000$ and $I_2 = 50$. The time spectra for each individual time constant are shown by the dotted and dashed line. The time resolution function is approximated by a single Gaussian function with $\sigma_t = 100$ ps. The background intensity I_b is set to 1.

2.4.2 Methods for positron production

Positrons can be produced by radioactive decay or by pair production.

Radioactive positron emitters exist of nuclei that have too many protons for stability and therefore they often decay by changing a proton into a neutron. This type of decay releases a positron e^+ and an electron neutrino ν_e . The positron decay reaction can generally be written as:



The decay product $[{}^A_{Z-1}\text{D}]^-$ is a negative ion due to the changed proton. [14] For positron beam experiments, a sodium-22 source is usually preferred for its relatively long half-life of 2.602 y and a positron yield of 90.4% [2].

Positron pair production is a process where a positron electron pair are created by the absorption of a photon. This photon must have an energy of at least $E_\gamma = 2m_e c^2$. Where, m_e is the electron mass and c is the speed of light. Just as in the annihilation process, the momentum and energy are conserved.

A pair production positron generator must be designed in such a way that the positrons can be extracted out of the solid where they were produced. A material must be chosen with a negative positron work function. This allows the emission of positrons that reach the surface by diffusion. The generator must receive high energy photons in order for pair production to occur. These photons can for example be generated by a nuclear reactor or a high energy electron beam.

2.4.3 Positron moderator

The moderator is used to slow down the positrons to a known energy. Radioactive β^+ sources radiate positrons with a wide spectrum of energies. For achieving depth resolution in a measurement, the implantation profile must be known. The implantation profile depends on positron energy and the mass density of the sample. Therefore, a monoenergetic positron beam is preferred.

A moderator is made from a material that has a negative work function for positrons. This means that the electrostatic potential for positrons is greater within the moderator material than outside. Positrons that enter the moderator are rapidly thermalized and diffuse through the material. If the thermalized positrons diffuse out of the moderator, then they will be accelerated with an energy that equals the work function. For tungsten, the work function equals $\phi_+ = -3.0$ eV [15]. The total energy of the moderated positrons equals the thermal energy minus ϕ_+ . The thermal energy is relatively small and can be neglected for practical applications. The efficiency of the moderator η is defined as the maximum fraction of emitted thermalized positrons.

The geometry of the moderator can be a thin foil to allow the emission of positrons in the same direction as the incident beam. This is a transmission mode moderator. In a reflection mode moderator, the positrons diffuse out of the material in the opposite direction of the incident beam. In this case, the moderator can be a thick crystal, which is more durable.

3 Instruments and Methods

This chapter includes a general description of the positron instruments and explains the methods that were used in this project.

3.1 Instruments

Two positron instruments were used in this project:

- POSH-PALS intense positron beam lifetime spectrometer (Section 3.1.1),
- Variable Energy Positron facility (Section 3.1.2).

3.1.1 Intense Positron Beam lifetime spectrometer

In Figure 14 a drawing of the POSH-PALS facility is shown. This is an intense positron beam lifetime spectrometer and it makes use of the POSH source.

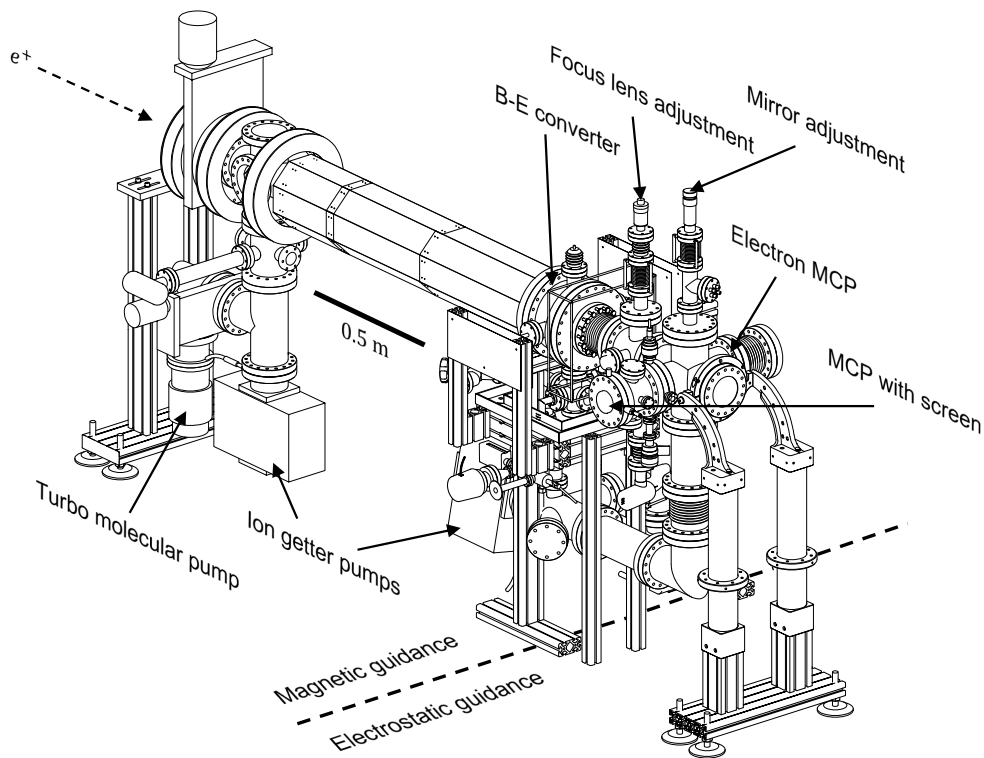


Figure 14: A 3D drawing of POSH-PALS facility. (CAD by M.R. de Boer and M. Butterling)

Positron transport

Positrons that are generated by the POSH source are magnetically guided in high vacuum beam tubes to the POSH-PALS facility. These tubes are wound with copper wire to induce the main magnetic field that is parallel to the intended travel direction of the positrons. The beam tubes are also equipped with horizontal and vertical correction coils to compensate for the Earth's magnetic field. The correction coils are also needed to keep the positrons on their path while traveling through a bent beam tube. The positrons enter the POSH-PALS facility through a straight beam tube which has an octagonal cover made from μ -metal. This part is shown in Figure 14.

Beam narrowing and positron moderation

After the straight beam tube, the positrons enter the B-E converter. A sectional drawing of the POSH-PALS apparatus including the B-E converter is shown in Figure 15.

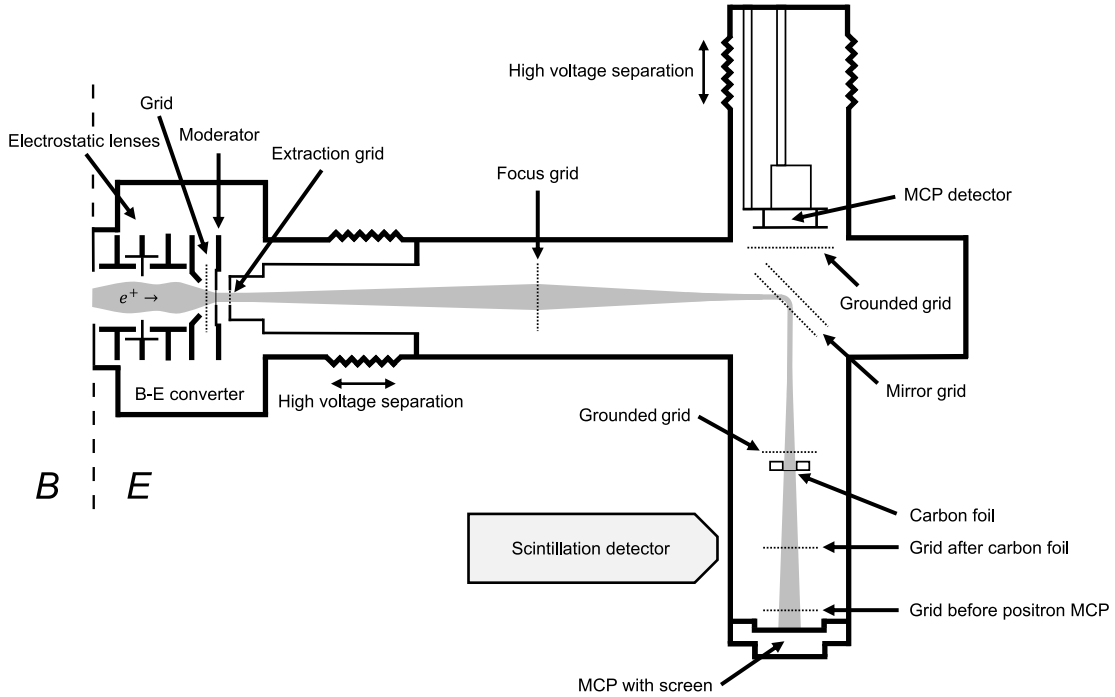


Figure 15: A sectional drawing of the electrostatic guidance part (E) of the POSH-PALS apparatus. The positron beam enters the apparatus from the magnetic guidance part (B) at the left. The beam is focused onto moderator foil. Moderated positrons are extracted by an extraction grid that is electrically connected to the right part of the apparatus. The mirror grid bends the positron beam with a right angle. Then, the positron beam goes through a carbon foil to generate secondary electrons. Finally, the positron beam is focused with two grids onto a MCP with a fluorescent screen.

Two things happen inside the B-E converter. First, the positrons endure a transition from magnetic to electrostatic guidance. Secondly, the positron beam is focused onto a single crystal 50 nm thick tungsten foil moderator. This moderates and narrows the positron beam. The moderator itself is charged to a specific voltage to achieve the optimum implantation energy.

The positrons are electrostatically extracted from the moderator by a charged grid. This accelerates the positrons to a desired energy and keeps the beam narrow. This extraction grid is charged negatively and is electrically coupled to the section of the vacuum chamber that is located behind it. Therefore, the positrons do not slow down after they pass the extraction grid. Within this vacuum chamber, the beam must be as narrow as possible to ensure that the variance in the time of flight is minimized.

Electrostatic mirror and secondary electron generation

A focus grid ensures that the beam is focused onto the mirror grid. The mirror grid will bend the beam with 90 degrees. It additionally functions as a low pass energy filter. The positrons will then travel further into a carbon foil which is positioned behind a grid that is connected to the local ground of the surrounding vacuum chamber. This grid has no focusing purposes for the positrons, but it extracts the secondary electrons that are generated while the positrons travel through the carbon foil. This grounded grid is placed in front of the carbon foil to extract the secondary electrons in opposite direction of the positron beam. The carbon foil itself is charged negatively. Detecting these secondary electrons gives a starting time to begin measuring the lifetime of the positron. A Microchannel Plate (MCP) detector is used to detect the secondary electrons. This detector is called the electron MCP. As shown in Figure 16, the MCP is located behind the mirror. The secondary electrons are accelerated to a greater energy than the positrons, therefore, the electrons will pass the electrostatic mirror with less deflection. By detecting

an electron with the MCP, the timer starts to measure the lifetime of the positron that released this electron.

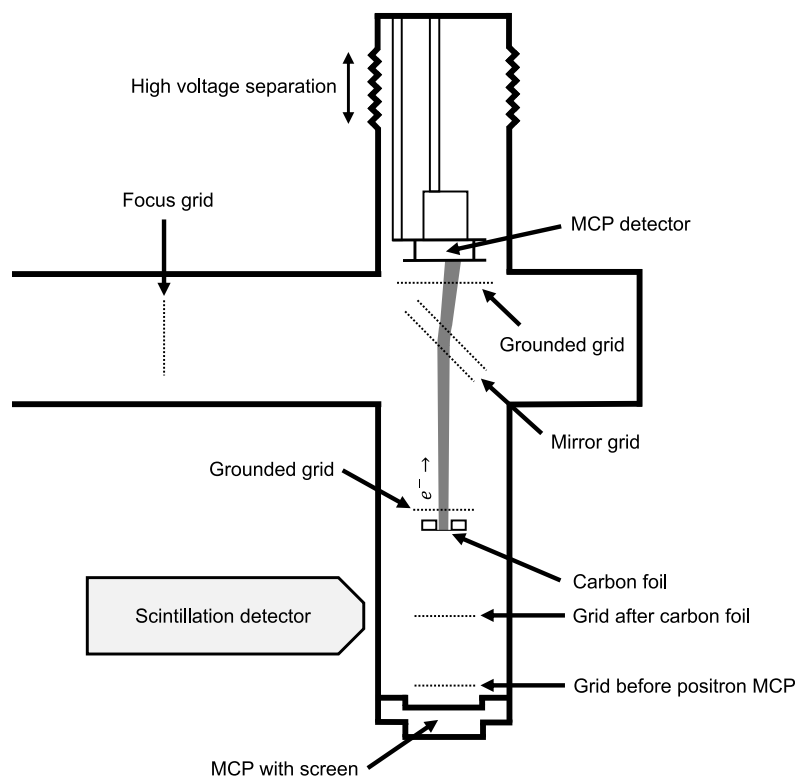


Figure 16: A sectional drawing of the secondary electron beam inside the the POSH-PALS apparatus.

MCP with fluorescent screen and scintillation detector

Once the positrons are transmitted through the carbon foil, they travel through two focus grids and end up into an MCP. This is another MCP which acts as a sample and can visualize the positron beam profile on a fluorescent screen. This device is called the positron MCP. Annihilation radiation is measured by a fast scintillation detector that is near the MCP, but outside of the vacuum chamber. A Pilot U scintillator is chosen for its fast decay time. Once the scintillation detector measures a 511 keV photon, the timer is stopped, and the lifetime is added to a histogram that will show the positron lifetime spectrum.

Measurement system

An Ortec 566 Time to Amplitude Converter (TAC) is used to measure the time between a pulse given by MCP and the scintillation detector. The TAC is configured to convert 0 to 50 ns into a 0 to 10 V. The output signal of the TAC is captured by a Personal Computer (PC) using an Analog to Digital Converter (ADC). A diagram of the connections is shown in Figure 17.

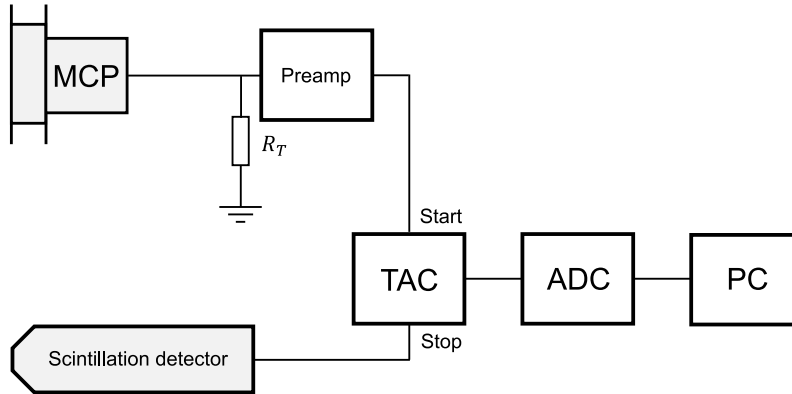


Figure 17: A diagram of the measurement system of the POSH-PALS facility.

The amplitude of the pulses of the MCP are not high enough to trigger the TAC. Therefore, a preamplifier was added near the MCP. Also, a $50\ \Omega$ terminator resistor was added to the input of the preamplifier to suppress reflections.

Positron Source

The POSH positron source is a device that emits positrons that are generated by pair formation in tungsten foils near the reactor core. The tungsten foils are arranged as a grid to achieve a large surface area. The Hoger Onderwijs Reactor (HOR) has multiple neutron beam tubes and one of them contains this positron source. By placing the positron source at the end of the beam tube, it benefits from the high intensity and high energy gamma radiation that is generated by the reactor core. The emitted positrons are guided magnetically by high vacuum beam tubes into the POSH-PALS facility.

This source is used for its property to deliver an intense positron beam with a relatively low energy with a mean value of 1.16 ± 0.20 keV. The low energy allows the use of an efficient 50 nm thin tungsten moderator foil that can have an efficiency of more than 10%. High activity ^{22}Na sources can deliver the same positron intensities, but generate a wide energy spectrum of fast positrons. Therefore, the moderator foil needs to be twenty times thicker to slow down the fast positrons. This gives a low efficiency of about 0.01%.

3.1.2 Variable Energy Positron facility

The VEP apparatus is an instrument that is able to generate a monoenergetic positron beam using a ^{22}Na source. The positron energy can range from 0.1 to 25 keV. The positron beam is implanted into a sample. The annihilation radiation coming off the sample is measured by a High Purity Germanium (HPGe) detector. A measurement gives the 511 keV peak count rate, the S- and W-parameter and the emitted positronium fraction of the sample versus the implantation energy.

In this project, the VEP facility will be used to determine the efficiency of 50 nm tungsten moderator foils. For determining the efficiency of moderator foils, only the peak count rate is of interest. This is further explained in section 3.2.3.

Monoenergetic positron beam generation

The ^{22}Na source generates a spectrum of positron energies, therefore the positrons pass through a tungsten foil moderator. The moderated positrons have a kinetic energy of 3.0 eV [15] plus their negligible thermal energy. Extraction grids are positioned behind the moderator to create a straight beam of positrons. Positrons have the possibility to be transmitted through the moderator without being fully thermalized. Therefore, the positrons pass through a bent section of the instrument where the magnetic field filters out incorrect energies. The positrons which passed the filter are electronically accelerated to the configured energy. The complete vacuum chamber of the VEP facility has a magnetic field that is parallel to the intended positron travel direction. This magnetic field is induced by a series of Helmholtz coils. A sectional drawing of this part of the VEP facility is shown in Figure 18.

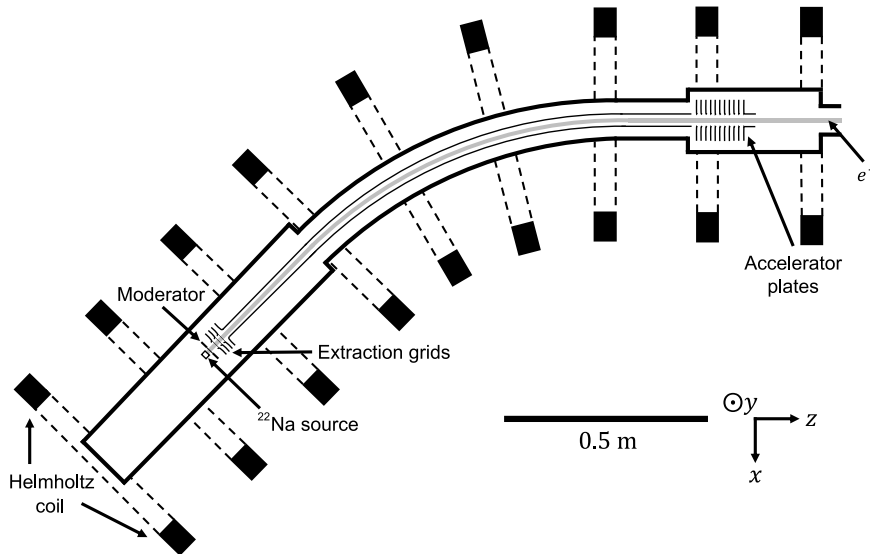


Figure 18: A sectional drawing of the first part of the VEP facility. At the left, a high vacuum chamber is shown that contains the ^{22}Na source. The emitted positrons go through a tungsten moderator foil. Grids extract the positrons from the moderator to produce a straight beam. The positron beam passes through a bent section of the vacuum chamber for energy filtering. The magnetic field in the bent section is tuned to pass the moderated positrons and reject the high energy ones. The main magnetic field is induced by Helmholtz coils. The moderator positrons pass through an accelerator to gain the kinetic energy that is desired for the experiment.

The vacuum chamber that holds the ^{22}Na source and the moderator is shielded with lead. Also, the bent section has lead shielding. The intensity of the moderated positron beam is low and therefore no lead shielding is placed on the other beam tubes.

Filters and sample holder

Before the positron beam hits the sample, it passes through an $\mathbf{E} \times \mathbf{B}$ -filter and a retarding field grid. This $\mathbf{E} \times \mathbf{B}$ -filter passes all positrons that go to the sample, but steers reflected, epithermal and thermal positrons from the sample into a beam dump. The next filter is a retarding field grid, which is usually charged with a voltage of ± 30 V. This grid can reflect or pass thermalized emitted positrons back into the sample. This grid is called the primary grid (G_1).

The sample holder can move in the y -direction to allow the measurement of multiple samples without removing the vacuum. It is moved by electric motor with a gear and screw reduction. A digital caliper measures the position of the sample holder.

Gyration adjustment coils

Positron beam widening oscillations were observed during the development of the VEP facility [6]. The beam widening oscillations are caused by the gyrating motion of the positrons while traveling in a magnetic field. These oscillations are acceleration energy dependent. The beam width at the sample holder can be minimized by controlling the gyration of the positrons with two Helmholtz coils. The electric current through these coils is adjusted if the accelerator voltage is changed.

Detector

The VEP facility uses a single High Purity Germanium (HPGe) detector for measuring the annihilation radiation. The detector is cooled cryogenically by liquid nitrogen. Therefore, the detector is mounted on a dewar for liquid nitrogen. The vacuum chamber has two thin metal windows located near the sample to allow the gamma photons to pass through to the detector. The second window allows the use of another HPGe detector for coincidence measurements. Coincidence measurements were not performed during this project due to an insufficient activity of the ^{22}Na source. A bin for Nuclear Instrumentation Modules (NIM) contains a high voltage power supply, an amplifier and an ADC for the HPGe detector.

Modifications for thin foil moderator characterization experiments

The VEP facility was modified to allow measurements of thin foil moderator samples that can transmit positrons. More information about the reason for these modifications can be found in Section 3.2.3. A straight 1 m high vacuum tube with a solenoid was attached to the end of the VEP facility. The tube was closed with a beam dump or a MCP detector. A glass view port was used as beam dump. A HPGe detector can be positioned near the beam dump to measure the annihilation radiation of the transmitted positrons. Additionally, a secondary retarding field grid (G_2) was installed right after the sample holder. A sectional drawing of a part of the VEP facility including the filters, sample and beam tube extension is shown in Figure 19.

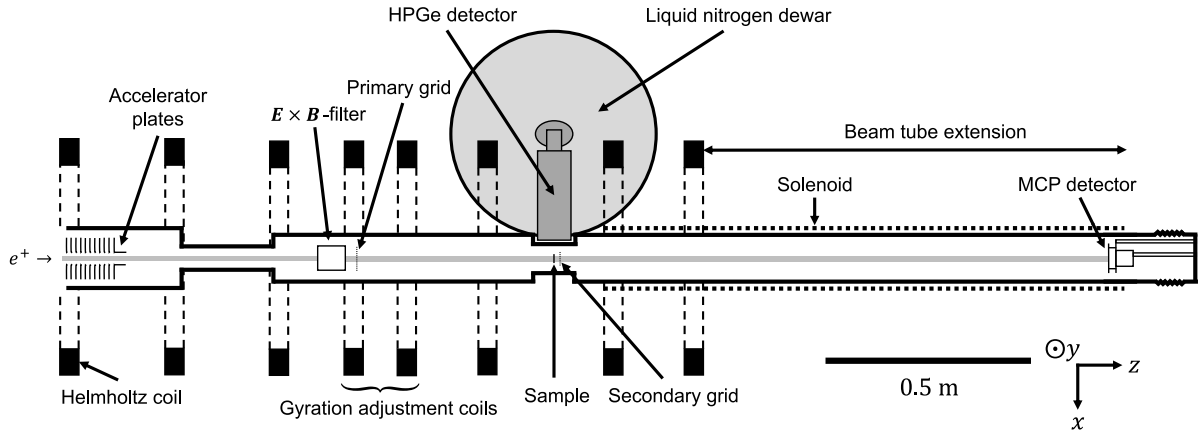


Figure 19: A sectional drawing of the second part of the VEP facility. The accelerated positrons go through an $\mathbf{E} \times \mathbf{B}$ -filter and the primary grid. The sample is positioned between two thin metal windows to allow the transmission of annihilation radiation to the HPGe detector. The secondary grid is positioned right behind the sample. Positrons that are transmitted through the sample travel further in a long beam tube to a MCP detector.

A complete drawing of the VEP facility can be found in Appendix D.

3.2 Methods

The main research goal of this project is to further develop the POSH-PALS facility such that it is able to measure a positron lifetime spectrum. Multiple adaptations and tests had to be done in order to achieve this goal. The flowchart shown in Figure 20 provides an overview of the complete project.

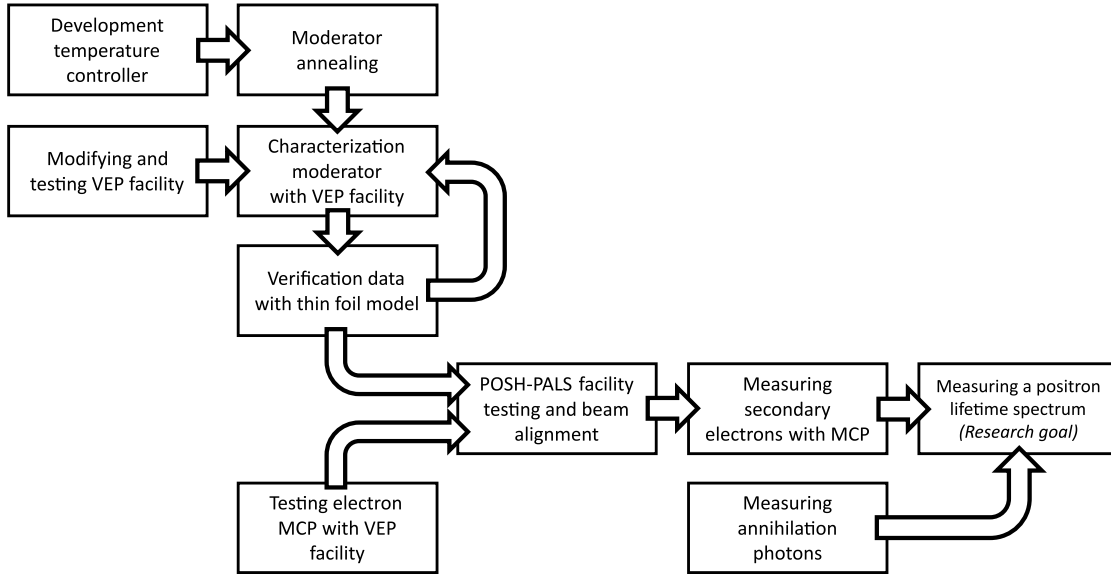


Figure 20: A flowchart of all the tasks that had to be completed in order to measure a positron lifetime spectrum with the intense positron beam lifetime spectrometer.

At the start of the project, the POSH-PALS facility could not deliver a thermalized positron beam from its moderator. The problem was solved by reannealing this moderator. Additionally, a new moderator was prepared and annealed. These moderators were annealed in a high temperature oven in vacuum. A controller was developed to control and measure the temperature of the oven.

→ The temperature curves of the annealing process can be seen in Section 4.2.1.

The VEP facility was used to perform characterization measurements on the moderators. The results from these measurements give information about the efficiency, the positron emission branching ratio and the effective diffusion length. At the same time, the thin foil model was developed to verify the characterization measurement results.

The first VEP measurement of the moderator was performed with the high temperature oven as sample holder. The thin foil model helped to identify that the oven was interfering with the positron beam. Once, the oven was replaced by the original sample holder, the similarity between the measurement results and the thin foil model was greatly improved.

→ The results of the thin foil model can be seen in Section 4.2.2. The results of the characterization experiments with the VEP facility are shown in Section 4.2.3 and 4.2.4.

Once the moderator was ready, it was installed into the POSH-PALS facility. Afterwards, the positron beam was aligned. The alignment of the positron beam is a time-consuming process due to the many settings of the instrument that can be configured.

→ The results of the beam alignment can be seen in Section 4.3.1.

While the positron beam was being aligned, the scintillation detector was configured and tested. The last steps were to measure secondary electrons with the MCP detector and to measure a positron lifetime spectrum.

→ The detector testing results together with verification measurements of the VEP facility can be seen in Section 4.1. A positron lifetime measurement using the POSH-PALS facility is shown in Section 4.3.2.

3.2.1 Positron moderators

Two 50 nm thick and monocrystalline tungsten foil positron moderators were utilized in POSH-PALS facility during this project. The 50 nm tungsten foils were fabricated at the Aarhus University in Denmark. The first moderator was named W2022A and was already used in a previous experiment, but then, it did not generate enough thermalized positrons. The second moderator named W2022B was prepared with new tungsten foil. The foils are delicate and therefore rest on a ring with a hexagonal mesh made from molybdenum to support them mechanically. A drawing of a grid ring is shown in Figure 21.

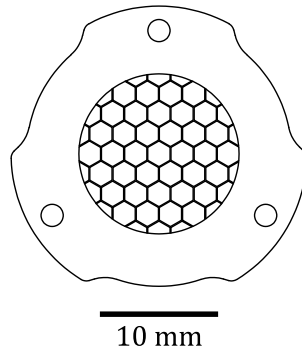


Figure 21: A drawing of a molybdenum grid ring.

These grid rings are mounted into the facilities by three screw holes and a tapered edge. Details about placing a tungsten foil onto a grid ring can be found in Appendix B. A photograph for each moderator was taken and is shown in Figure 22.

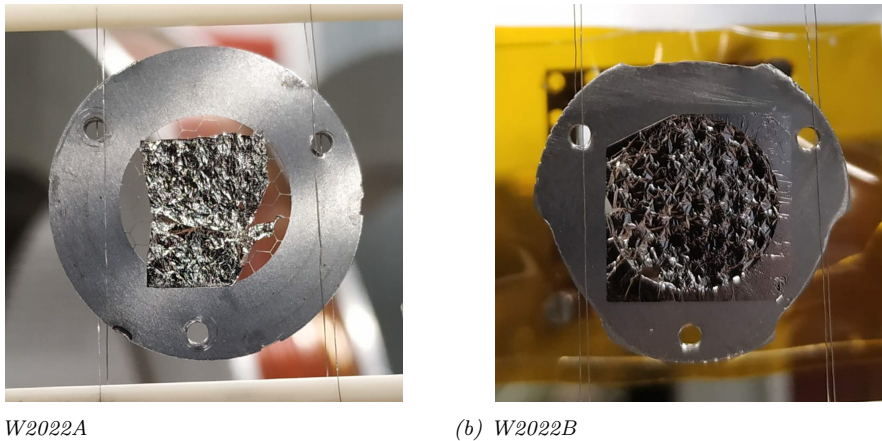


Figure 22: Photographs of moderator W2022A and W2022B. Both moderators have a specified thickness of 50 nm. The moderators rest on a molybdenum grid ring.

The efficiency of the moderators is improved by removing defects and impurities from the foil. This increases the effective diffusion length L_+ and the thermalized positron emission branching ratio ϵ_{e^+} . Defects and impurities are removed by heating the foil in a high temperature oven. Tungsten is chosen for its negative ϕ_+ and its high melting temperature. Therefore, the temperature can be maximized to remove the most impurities.

3.2.2 Moderator annealing

The moderators were annealed by a high temperature oven in high vacuum. This oven is made from a ceramic tube which is wound by heating wire. Instead of cables, electric current is delivered by molybdenum rods. These rods also support the oven mechanically. The electric power is provided by a Delta Elektronika SM 70 - 22 DC power supply. In Figure 23, photograph is shown of the high temperature oven while moderator W2022B was being annealed.

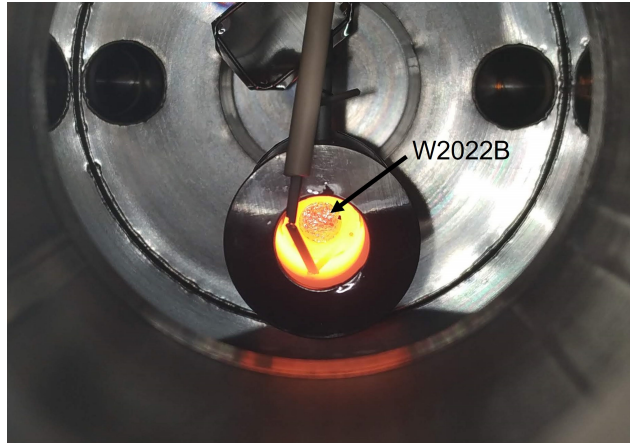


Figure 23: A photograph showing the high temperature oven annealing moderator W2022B at $T = 1094 \pm 10$ °C in a high vacuum chamber.

A constant temperature is maintained by a closed feedback loop oven controller. This controller, which measures the temperature near the moderator with a type C thermocouple and controls the output voltage of the power supply. More information about the temperature controller that was developed can be found in Appendix C.

The moderators were annealed at a target temperature of $T = 1100$ °C for a time of at least 15 minutes. The vacuum chamber can reach a minimum pressure of $< 10^{-7}$ mbar.

3.2.3 Moderator characterization method

The moderators are characterized by positron annihilation and transmission measurements using the VEP facility. For these experiments, the VEP facility had to be modified to allow the transmission of positrons through the foil. Usually, thick (~ 1 mm) samples are loaded into the VEP facility that do not allow the transmission of positrons. If positrons are transmitted, then they would be implanted right behind the sample into the vacuum chamber wall. This would give annihilation radiation which does not originate from the moderator. The solution is to extend the beam tube behind the sample holder. The tube allows the positrons to travel further and be annihilated at a beam dump that is relatively far from the HPGe detector. This tube extension allowed the placement of a second HPGe detector that measures the annihilation radiation of the transmitted positrons. This second detector can also be a MCP detector.

The VEP facility has the capability to charge the primary grid (G_1) that is located in front of the sample with a voltage of ± 30.0 V. Another similar grid called the secondary grid (G_2) has been mounted behind the sample. Charging these grids with $+30.0$ V reflects all positrons with an energy that is less than 30.0 eV back to the sample. A voltage of -30.0 V passes all positrons.

For an annihilation measurement, two measurements are performed for a primary grid voltage of $V_{G1} = \pm 30.0$ V. A HPGe detector near the sample detects the annihilation radiation. Grid G_2 is charged to a voltage of $V_{G2} = -30.0$ V.

For a transmission measurement, a MCP or a HPGe detector is located at the end of the beam tube. The MCP detector directly measures the transmitted positrons. The HPGe detector measures the annihilation radiation coming from transmitted positrons that end up in a beam dump. Grid G_1 is set to a voltage of $V_{G1} = +30.0$ V and G_2 is switched to $V_{G2} = \pm 30.0$ V. The measurement setup for an annihilation and transmission measurement for positive grid voltages is visualized in Figure 24.

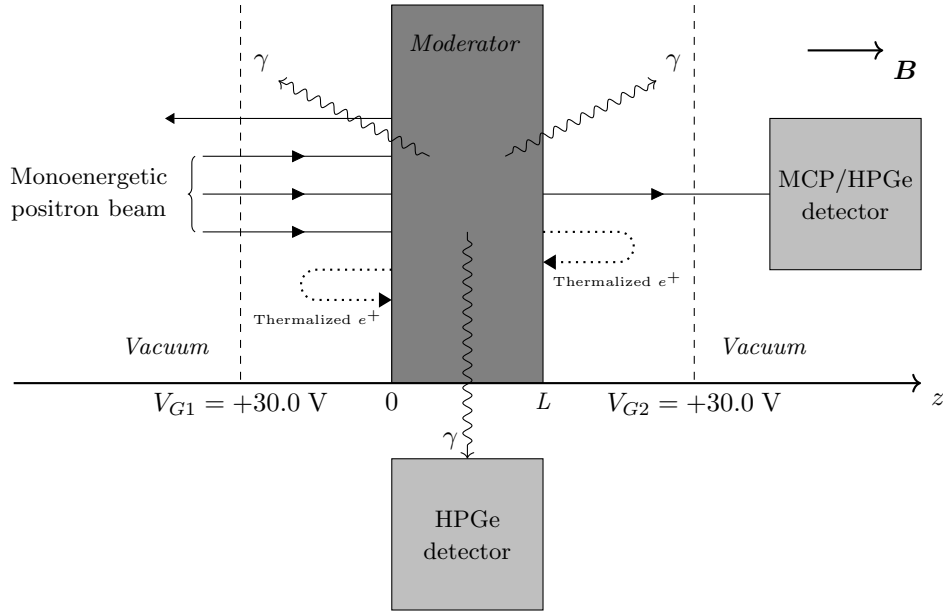


Figure 24: A simplified drawing of characterization measurement setup for positron moderators. A variable and monoenergetic positron beam is aimed onto the moderator. Positron annihilation within the moderator emits 511 keV γ -photons. A HPGe detector near the moderator detects these photons. The moderator is placed between the primary and secondary grid which are in this case charged with a voltage of +30.0 V. Therefore, the emitted thermalized positrons are reflected back into the moderator. Positrons with a kinetic energy greater than 30.0 eV can pass the grid potentials. The transmitted positrons which pass the grid are detected by a MCP or HPGe detector. The moderator is located within a beam tube with a magnetic field \mathbf{B} .

The fraction of thermalized positrons emitted from the rear surface of the moderator F_{re+} is the normalized count rate difference of a transmission measurement when G_2 is switched to ± 30 V:

$$F_{re+} = \frac{R_{G2-} - R_{G2+}}{R_0}. \quad (41)$$

In this equation,

- F_{re+} is the fraction of emitted thermalized positron from the rear surface of the moderator.
- R_{G2-} is the count rate measured with G_2 set to a voltage of -30 V,
- R_{G2+} is the count rate measured with G_2 set to a voltage of $+30$ V,
- R_0 is the count rate of the incident positron beam.

These values are implantation energy dependent. At the optimum implantation energy E_{opt} , the maximum value of F_{re+} is reached. This is also defined as the moderator efficiency η . The error of F_{re+} is given by:

$$\Delta F_{re+} = F_{re+} \left[\frac{\Delta R_0}{R_0} + \frac{\sqrt{\Delta R_{G2-}^2 + \Delta R_{G2+}^2}}{R_{G2-} - R_{G2+}} \right] \quad (42)$$

The error of the count rate itself is calculated with the standard error:

$$\Delta R = \sigma_R = \frac{\sqrt{N}}{t_m}, \quad (43)$$

where N is the number of counts and t_m is the measurement time.

3.2.4 Monoenergeticity and beam profile measurement of VEP facility

The VEP facility was modified by extending the beam tube. The monoenergeticity and beam profile were measured to ensure that this modification did not affect the characterization measurements of the moderators.

The monoenergeticity of the positron beam is measured by a retarding field experiment using grid G_1 that is located before the sample holder. A MCP detector which is mounted behind grid G_1 , measures the intensity of the positron beam. The accelerator is connected to a precision DC power supply instead of the high voltage power supply. Disconnecting the high voltage power supply, allows the use of an ordinary multimeter to measure the voltage of the accelerator. Once the accelerator is set to a constant voltage in the order of 100 V, the count rate of the MCP is measured while stepwise increasing the voltage of G_1 . If the potential G_1 is great enough, the positrons will be deflected back and the count rate of the MCP will lower. The derivative of count rate versus the grid voltage gives the energy spectrum of the positron beam.

The beam profile was measured in two steps. The first step was to attach a MCP with a fluorescent screen to the end of the beam tube. The image directly shows the shape of the beam in both the x - and y -direction. However, it does not give any information about the beam width at the location of the sample holder. The second step was to measure the transmitted positron beam while stepwise moving some samples through the beam in the y -direction. This measurement gives the count rate versus the y -position of the sample holder. This measurement is a convolution of the beam profile and the shape of the sample holder. Therefore, the beam profile in the y -direction can be resolved from the data.

3.2.5 Detector testing

Microchannel plate detector

A Hamamatsu F9890 MCP detector assembly was tested and used for experiments on the VEP facility. This detector has the capability to detect electrons, positrons and other charged particles in high vacuum chambers. A photograph of the MCP assembly attached to a high vacuum electrical isolator is shown in Figure 25.

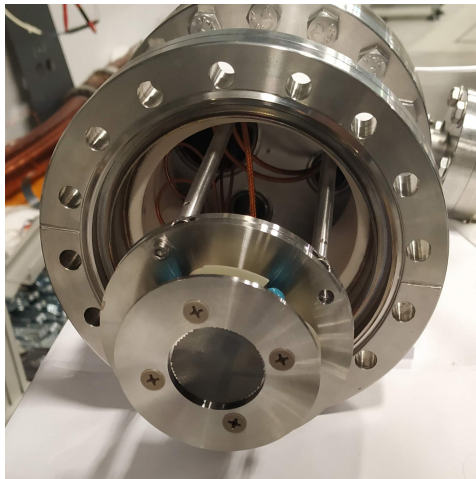


Figure 25: A photograph of the Hamamatsu F9890 microchannel plate detector assembly. Behind the MCP assembly, there is a high vacuum electrical isolator.

The purpose of this detector is to measure secondary electrons in the POSH-PALS facility. However, no electrical pulses from the MCP detector were measured in previous experiments. Therefore, the detector was temporarily moved to the VEP facility. In this facility, the MCP detector could be mounted on a position that is reachable for cable adjustments. This is not possible on the POSH-PALS facility due to unshielded high voltage components. Also, the reactor was not operational during these experiments. Therefore, the POSH source could not be used.

On the VEP facility, the MCP assembly was mounted at the end of the beam tube. Two Heinzinger PNC 3500-20 ump high voltage power supplies were used for powering the MCP assembly. The voltage

on the front of the MCP was set to $V_F = -1.96$ kV and back was grounded. The anode of the MCP was charged to $V_A = +0.60$ kV.

The output of the MCP assembly was connected to a Hamamatsu C5594 amplifier with a short SMA connector cable. This amplifier should have a $50\ \Omega$ input impedance, but it was found that adding a $50\ \Omega$ terminator resistor on the input reduced reflections. The output of the amplifier was connected to the start input of an Ortec 566 Time to Amplitude Converter (TAC). This TAC was the only device available that was able to convert the short electrical pulses from the MCP to longer pulses that the Analog to Digital Converter (ADC) could accept. Hence the need for a preamplifier to increase the pulse amplitude in order reach the threshold value of the TAC. The stop input of the TAC was connected to the start input with a 10 m long cable to artificially introduce a delay. The output of the TAC is connected to a Canberra 8077 ADC which itself was connected to a Personal Computer (PC). A schematic overview of the setup is shown in Figure 26.

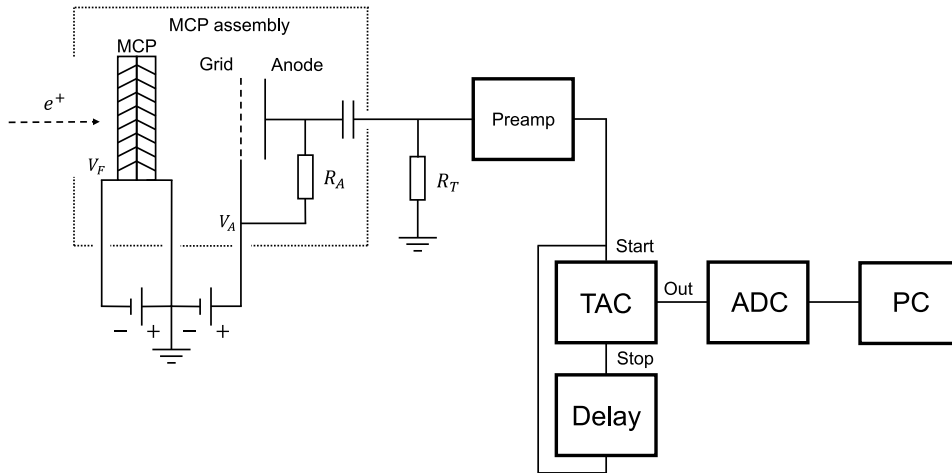


Figure 26: A schematic overview of the electronic connections to the MCP assembly. The MCP assembly itself is under vacuum. There is a terminator resistor of $R_T = 50\ \Omega$ attached to the input of the preamplifier for reducing its input impedance. The amplified signal goes to a Time to Amplitude Converter (TAC) which has the sole purpose to widen pulses. The start and stop inputs are connected to each other with a 10 m cable to create a delay. The output of the TAC is connected to an Analog to Digital Converter (ADC). The ADC itself is connected to a Personal Computer (PC) to log the measurement.

Scintillation detector

A fast scintillation detector with a Pilot U scintillator is installed on the POSH-PALS facility. This detector has photomultiplier tube that is shielded with μ -metal. Furthermore, the output signal of the photomultiplier tube is connected to one of its dynodes. Therefore, no constant fraction discriminator is needed to generate a zero-crossing point. Additionally, the detector has a build-in fast Single Channel Analyzer (SCA). In Figure 27, a photograph of the scintillation detector is shown.

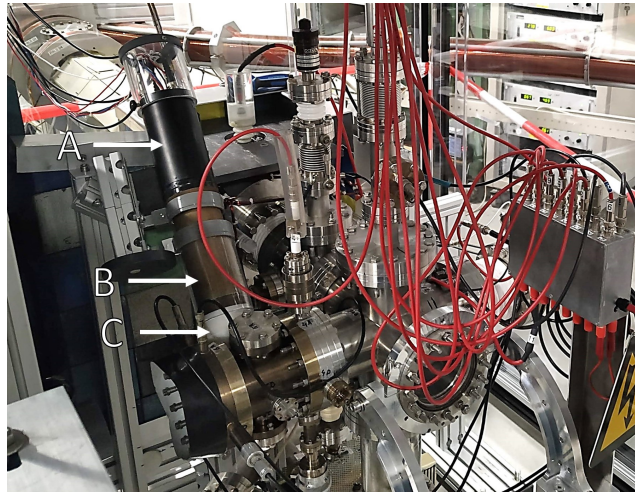


Figure 27: A photograph of the fast scintillation detector installed on the POSH-PALS facility. This detector has a build-in single channel analyzer (A). The photo multiplier tube (B) is shielded with μ -metal. The scintillator (C) is located under a plastic cap.

The scintillation detector was tested with annihilation radiation coming from the POSH-PALS facility. This has the benefit that most gamma photons have an energy of 511 keV, which makes the configuration of the SCA easier.

4 Results and Discussion

In this chapter, the measurement results are shown that prove that the positron moderators, the VEP facility and the POSH-PALS facility work as intended. In Section 4.1, proof of correct functioning of the MCP detector and the fast scintillation detector are shown. Furthermore, the profile and monoenergeticity of the positron beam from VEP facility is analyzed. All moderator characterization results are shown in Section 4.2. Lastly, the first ever positron lifetime spectrum measured by the POSH-PALS facility is presented in Section 4.3.

4.1 Instrument verification

This section includes the verification results of the:

- Microchannel plate detector,
- Scintillation detector,
- Variable Energy Positron facility.

4.1.1 Microchannel plate detector

The Hamamatsu F9890 MCP detector assembly was tested with positrons from the VEP facility and secondary electrons that were generated by the POSH-PALS facility. The voltage on the front of the MCP was set to $V_F = -1.96$ kV and the back was grounded. The anode of the MCP was charged to a voltage of $V_A = +0.60$ kV. The output signal from the anode was preamplified near the detector.

In Figure 28, a single pulse from the MCP detector while measuring secondary electrons is shown. This was measured with a Teledyne LeCroy HDO9404 oscilloscope with a bandwidth of 4 GHz.

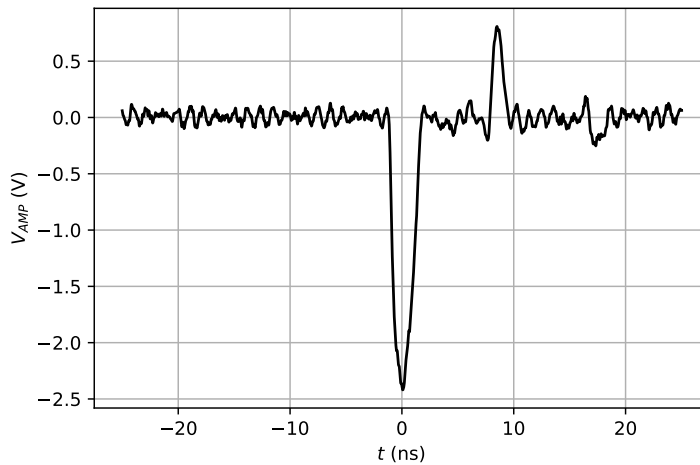


Figure 28: An amplified voltage pulse that is generated by the microchannel plate detector. The plot shows the measured voltage V_{AMP} versus the time t .

This result shows that the MCP detector and the preamplifier function properly. Without the preamplifier, the negative pulses had a measured amplitude of less than 100 mV and a full width half maximum (FWHM) of less than 1 ns. The amplified signal has a FWHM of 1.9 ns. The MCP detector produced similar results when detecting positrons from the VEP facility. Additionally, the experiments on the VEP facility have shown that the sensitivity of the MCP detector is energy dependent.

4.1.2 Scintillation detector

The fast scintillation detector was tested with 511 keV photons from the POSH-PALS facility. This detector has a special photomultiplier tube where the output signal is measured from one of its dynodes instead of the detector plate. Such a photomultiplier tube outputs a characteristic time dependent voltage oscillation. The voltage on the photomultiplier tube was set to $V_{PMT} = -2.05$ kV. In Figure 29, this oscillation is clearly measured by the oscilloscope.

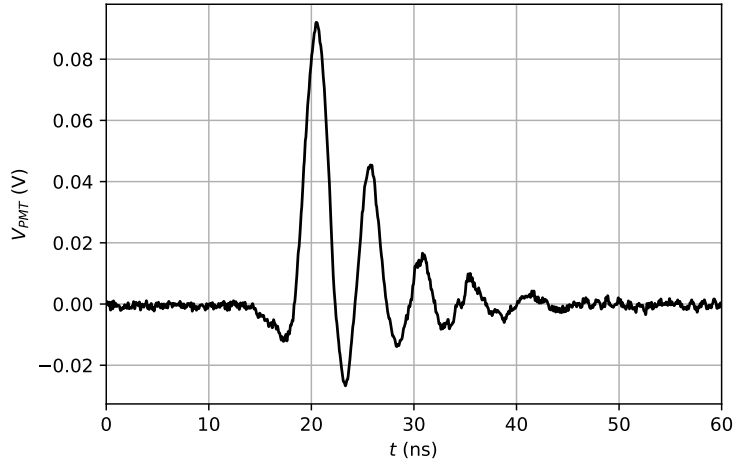


Figure 29: A voltage pulse that is generated by the scintillation detector. The plot shows the measured voltage V_{PMT} versus the time t .

This shows that the scintillation detector is functioning correctly. Furthermore, the upper and lower level and walk adjust were configured to analyze nearly the complete measurable spectrum to prioritize count rate over time resolution.

4.1.3 Variable Energy Positron facility

The profile, position and monoenergeticity of the positron beam from the VEP facility were analyzed after it was modified by extending the beam tube. This was necessary to ensure that the characterization experiments of the moderators were performed correctly.

Positron beam profile and position analysis

Beam profile measurements were performed on the VEP facility. This was necessary to ensure that the positron beam will precisely hit the sample after the facility was extended with a long tube. At the end of this tube, a MCP with a phosphor screen was mounted. The voltage of the front, back and screen of the MCP were set to -1.85 kV, 0.0 V and 2.75 kV respectively. Due to the low positron flux, the detected beam was not visible on the screen to the naked eye. This problem was solved by making long exposure photographs of the MCP screen. Multiple photographs were taken to observe the positron beam while tuning the settings of the instrument. To center the beam onto the MCP, the electric current through the horizontal and vertical correction coils were set to $I_H = -0.26$ A and $I_V = 1.77$ A respectively. This resulted in the centered beam that is shown in Figure 30. In this figure, the positron beam was set to have an energy of 4.5 keV.

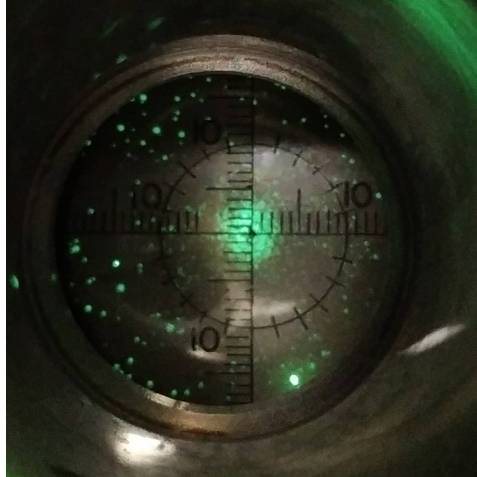


Figure 30: A long exposure photograph of the MCP screen. The screen shows, that the positron beam of the VEP facility is round and centered.

The detector shows that the profile of the positron beam is round. This measurement does not indicate the beam diameter and position at the sample holder. Another technique was used, where the beam intensity was measured while stepwise moving the sample holder.

The sample holder was loaded with two molybdenum grids and two ceramic rods. One of those grids was equipped with moderator W2022A. A photograph of this sample holder is show in Figure 31.

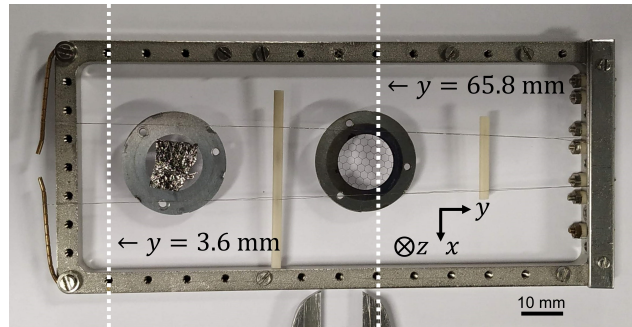


Figure 31: The sample holder of the VEP facility loaded with multiple objects. From left to right, the positron moderator W2022A was mounted first, followed by a ceramic rod, a molybdenum grid ring and another ceramic rod. The sample holder is photographed horizontally, but it is held and moved vertically between the vertical dotted lines in the VEP facility.

A positron transmission measurement was performed while moving the sample holder from $y = 3.6$ mm to 65.8 mm in steps of about 0.5 mm. This range is indicated in Figure 31. Each step has a measurement time of $t = 10.0$ s. The transmitted positrons were measured with a MCP detector assembly. For this MCP detector, the voltage of the front, back and the anode were set to -1.96 kV, 0.0 V and 0.60 kV respectively. The count rate of the MCP detector R_{MCP} was measured versus the sample position y . In order to resolve the beam width, this data was fitted with a convolution of the expected shape of the samples $f_{shape}(y)$ and a Gaussian function:

$$R_{fit}(y) = f_{shape}(y) * \left[\frac{1}{\sigma\sqrt{2\pi}} \exp\left(\frac{-y^2}{2\sigma_w^2}\right) \right]. \quad (44)$$

This Gaussian function is a parameterization of the beam profile. The function f_{shape} consists of multiple square functions that together parameterize the objects on the sample holder that is shown in Figure 31. The transmission of the positron beam measured by the MCP detector versus the sample position is shown in Figure 32. This transmission curve is fitted with Equation 44.

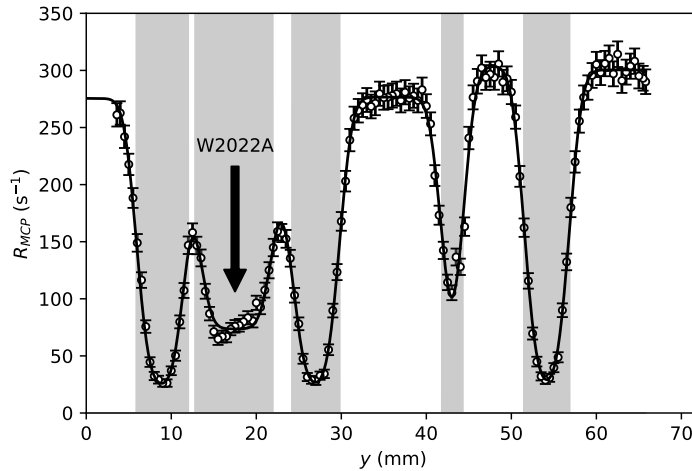


Figure 32: A plot of the count rate of the transmitted positron beam R_{MCP} versus the sample position y . The data is fitted with a convolution of the shape of the sample and a Gaussian function with $\sigma_w = 1.2$ mm. This Gaussian function parameterizes the positron beam profile. The shape of the sample is indicated by the grey vertical bars. The indicated count rate error equals the 2σ standard deviation.

This measurement shows that positron beam can be parameterized by a Gaussian function with $\sigma_w = 1.2$ mm. Therefore, the FWHM of the beam equals $w = 2.8$ mm. This is smaller than the diameter of the moderator foils, which is approximately 10 mm for W2022A and 13 mm for W2022B.

Another transmission measurement was performed on the same samples with variable positron energy. An intensity plot of R_{MCP} versus y and the positron acceleration energy E_a is shown in Figure 33.

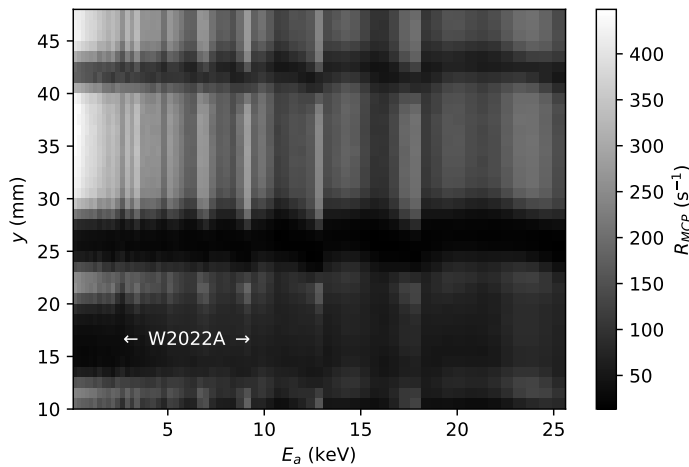


Figure 33: An intensity plot of the count rate of the transmitted positron beam R_{MCP} versus the sample position y and positron acceleration energy E_a .

This result shows that the MCP detector has a reduced sensitivity at higher positron energies. Also, there are energy depended oscillations present in the count rate and the sample position. These oscillations are caused by a pair of Helmholtz coils that alter the gyration radius of the positrons in such a way that the beam width is minimal at the sample location. The electric current through these coils is determined by a non-continuous function which itself depends on the accelerator voltage. The oscillations can be reduced by redefining this function. This is a time-consuming process and is not in the scope of the project. Therefore, the adjustments to the vertical and horizontal correction coils were undone. The original correction coil settings are; $I_H = 0.00$ A and $I_V = 0.52$ A.

Resetting the correction coils settings reduced the energy and positional amplitude of the oscillations. Furthermore, σ_w remained the same.

Monoenergeticity of the positron beam

A retarding field experiment was performed on the positron beam of the VEP facility. With this experiment, the monoenergeticity of the positron beam is measured. For this experiment, a retarding field grid was activated between the positron source and a MCP detector. If the accelerating voltage is greater than the voltage of the retarding field grid, then the positrons will be transmitted to the MCP detector. Otherwise, the positrons will be reflected by the grid.

The retarding field was generated by the primary grid G_1 . The voltage on this grid V_{G1} was stepwise increased from 10.0 to 150.0 V. The configured positron acceleration voltage V_a was set to 99.4 ± 0.1 V. The measured MCP detector count rate R_{MCP} versus the primary grid voltage V_{G1} is shown in Figure 34.

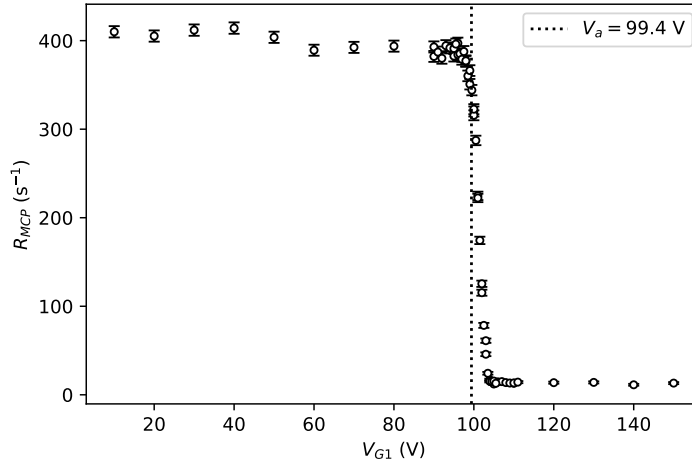


Figure 34: The count rate of the MCP detector R_{MCP} versus the primary grid voltage V_{G1} . Each point has a measurement time of 10 s with dead time compensation. The acceleration voltage was set on $V_a = 99.4 \pm 0.1$ V. The indicated count rate error equals the 1σ standard deviation.

The measurement shown in Figure 34 reassembles the error function. Therefore, its derivative can be parameterized by a Gaussian function:

$$g(V_{G1}) = a \exp\left(\frac{-(V_{G1} - \mu)^2}{2\sigma_V^2}\right). \quad (45)$$

The derivative of $R_{MCP}(V_{G1})$ fitted with a Gaussian function is shown in Figure 35.

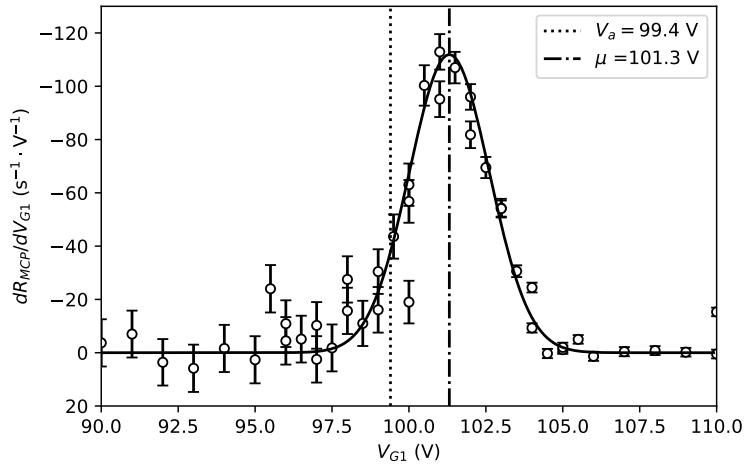


Figure 35: The numerically determined derivative of the count rate of the MCP detector R_{MCP} versus the primary grid voltage V_{G1} . The acceleration voltage was set to $V_a = 99.4 \pm 0.1$ V. The data was fitted with a Gaussian function where $a = -111.9 \text{ s}^{-1} \cdot \text{V}^{-1}$, $\mu = 101.3$ V and $\sigma_V = 1.3$ V. The indicated count rate error equals the 1σ standard deviation.

This result shows that the actual positron beam energy, $E_\mu = 101.3$ eV, with a variance of $\sigma_E = 1.3$ eV, is greater than the acceleration energy, $E_a = 99.4 \pm 0.1$ eV. This gives a difference of $\Delta E = 1.9$ eV. It is expected that this additional energy positron is generated by the difference in work functions between the positron moderator and the retarding field grid. If the positron beam is implanted into a sample, ΔE could be different.

4.2 Moderator characterization

This section includes the results from the:

- Annealing of the moderators,
- Thin foil model simulation,
- Measurement of positron annihilation in the moderator,
- Measurement of positron transmission through the moderator.

4.2.1 Annealing of the moderators

Both moderator W2022A and W2022B were annealed in a high temperature oven in vacuum ($< 10^{-5}$ mbar). The oven was controlled by a temperature controller and the maximum setpoint temperature was set to $T = 1100$ °C. A multimeter was connected to the thermocouple to verify if this temperature was reached.

For annealing moderator W2022A, the high temperature oven was installed into the VEP facility as a high vacuum chamber. The temperature versus the time is shown in Figure 36. In this figure, the curve itself was measured by the temperature controller without cold junction correction. The intersection of the dashed lines indicates the absolute temperature that was measured by the multimeter with cold junction correction in that point in time.

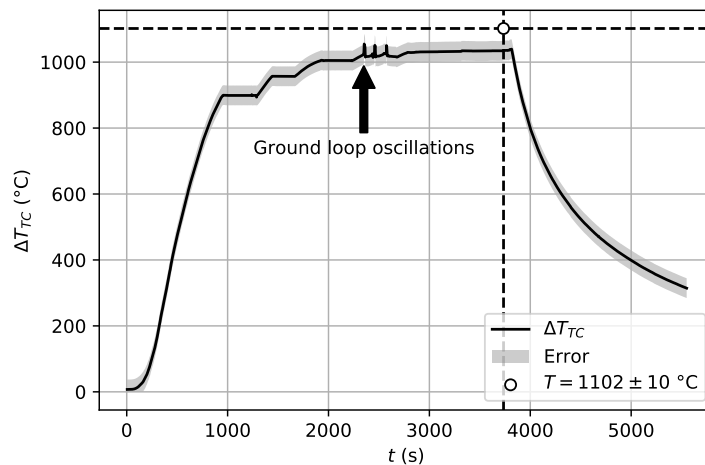


Figure 36: The measured temperature difference between the oven and the cold junction in time. Due to a ground loop, the measured temperature difference started to oscillate at $t \approx 2330$ s. The oscillation stopped by manually controlling the oven. The oven was manually kept on a temperature of 1100 °C for 15 minutes. At $t = 3735$ s, the oven reached an absolute temperature of $T = 1102 \pm 10$ °C.

The ground loop oscillations were caused by an electrical leakage current between the thermocouple and the heating wire of the oven. This can be solved by improving the electrical isolation within the oven or by installing an isolation amplifier between the oven controller and the power supply.

For annealing moderator W2022B, the high temperature oven was installed in another high vacuum chamber with a smaller vacuum pump. This vacuum pump could not maintain a proper vacuum while quickly heating the oven. A pressure increase was caused by the outgassing of the oven and moderator. Therefore, the heating of the oven was stopped temporarily at some intervals to maintain enough vacuum. The temperature versus the time is shown in Figure 37.

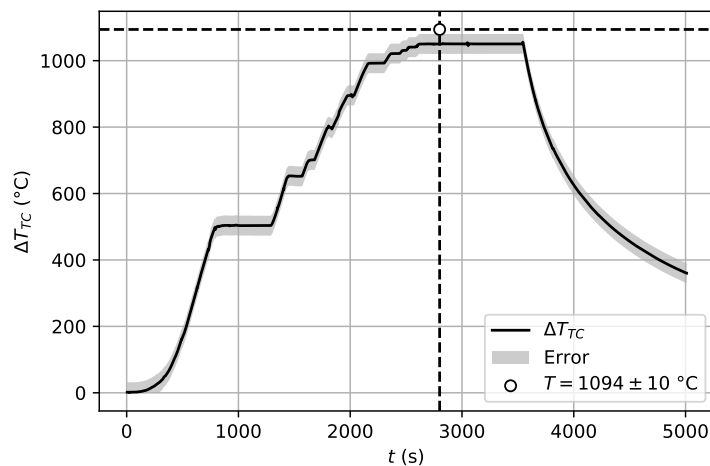


Figure 37: The measured temperature difference between the oven and the cold junction versus the time. The maximum absolute temperature of $T = 1094 \pm 10$ °C was kept constant for 15 minutes.

Both figures 36 and 37 show that the annealing temperature of 1100 ± 10 °C was reached and maintained for at least 15 minutes. This concludes that the annealing process was performed as intended.

4.2.2 Thin foil model simulation

Before the moderators were characterized by the VEP facility, the expected measurement results were simulated with the thin foil model. The simulation results helped understanding the annihilation and transmission measurements of the moderator foils. The parameters needed for running the simulation were chosen for a 50 nm foil with good moderator properties. A list of all simulation parameters is shown in Table 2.

Table 2: The chosen parameters for the thin foil model.

Foil thickness	L	50 nm
Effective diffusion length	L_+	50 nm
Bulk annihilation rate	λ_b	10^{10} s^{-1}
Specific trapping rate for defects	ν_t	10^{15} s^{-1}
Defect concentration	n_t	3×10^{-5}
Positron emission branching ratio (ϵ_{e+})	$\epsilon_{fe+} = \epsilon_{re+}$	1/3
Surface bound branching ratio (ϵ_{sb})	$\epsilon_{fsb} = \epsilon_{rsb}$	1/3
Positronium branching ratio (ϵ_{Ps})	$\epsilon_{fPs} = \epsilon_{rPs}$	1/3
Epithermal scattering length	l_{epi}	0.1 nm
Makhov parameters [12]	n	1.62
	α	$4.0 \text{ } \mu\text{g} \cdot \text{cm}^{-2} \cdot \text{keV}^{-1.62}$
	m	2.0

The simulation numerically integrates Equation 27 to get the steady-state thermalized positron concentration $c(z, E)$. This is shown for three different implantation energies in Figure 38.

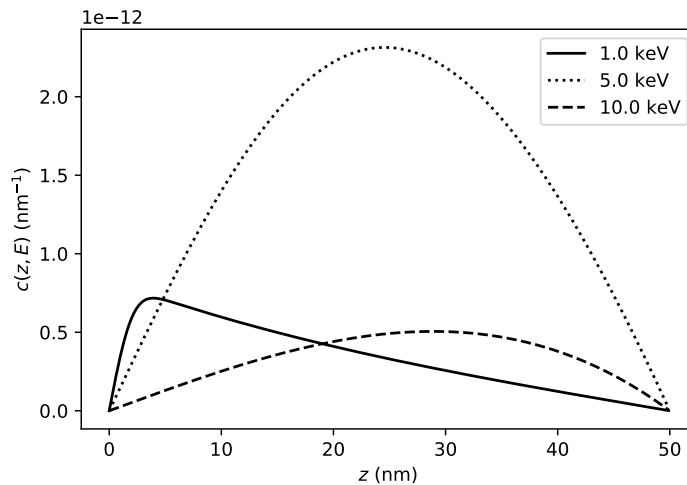


Figure 38: A plot of the simulated steady-state thermalized positron concentration $c(z, E)$ as a function of the spatial z -axis for three different implantation energies.

The two virtual detectors that are shown in Figure 5 simulate the detectors of the VEP facility. The virtual annihilation detector measures all annihilation radiation that originates from near or within the foil. This virtual detector mimics the side-mounted HPGe detector of the VEP facility. A plot of the simulated normalized count rate measured by the virtual annihilation detector versus the implantation energy is shown in Figure 39.

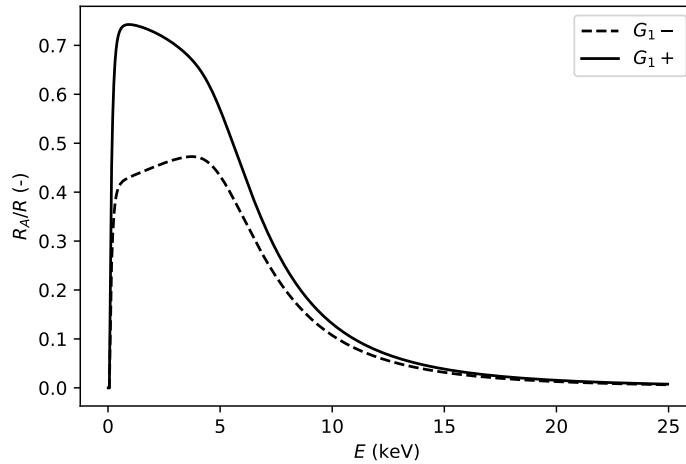


Figure 39: A plot of the simulated normalized count rate that is measured by the virtual annihilation detector as a function of implantation energy. The results are shown for a positive and negative charged primary grid G_1 . The secondary grid G_2 is charged negatively.

The virtual transmission detector mimics a HPGe or MCP detector which is mounted behind the foil. A plot of the simulated normalized count rate measured by the virtual transmission detector versus the implantation energy is shown in Figure 40.

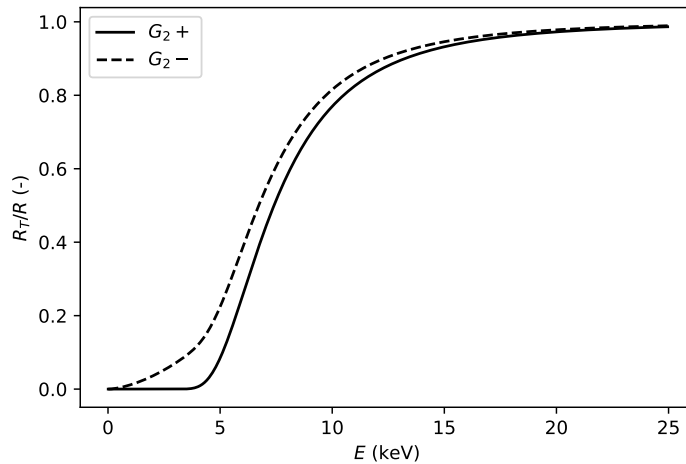


Figure 40: A plot of the simulated normalized count rate that is measured by the virtual transmission detector as a function of implantation energy. The results are shown for a positive and negative charged secondary grid G_2 . The primary grid G_1 is charged negatively.

Both figures 39 and 40 show a difference between the normalized count rate for a positive or negative charged grid. This difference equals backward or forward thermalized positron emission fraction. The difference in normalized count rate in Figure 39 gives the thermalized positron emission fraction from the front side of the foil F_{fe+} . The difference in normalized count rate in Figure 40 gives the thermalized positron emission fraction from the rear side of the foil F_{re+} . The simulated thermalized positron emission fractions from both sides of the foil versus the implantation energy are shown in Figure 41.

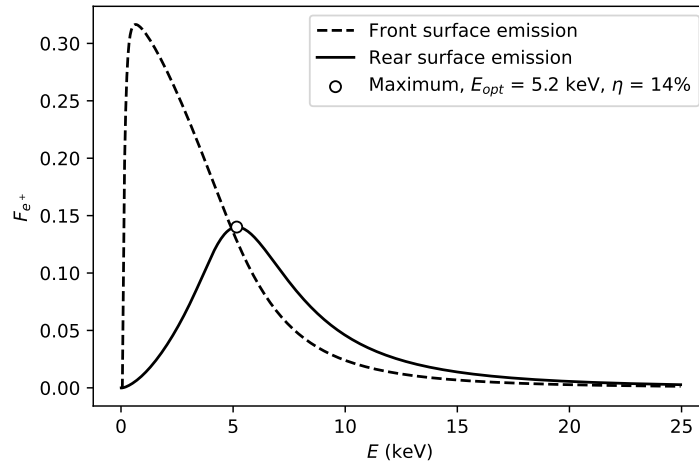


Figure 41: A plot of the simulated front and rear surface emitted thermalized positron fractions, F_{fe+} and F_{re+} , as function of implantation energy. The maximum number of thermalized positrons that are emitted from the rear surface of the foil is indicated in this graph. This maximum indicates that the simulated foil has a maximum efficiency of $\eta = 14\%$ at an implantation energy of $E = 5.2$ keV.

This result shows that simulated foil has a moderator efficiency of $\eta = 14\%$ at the optimum implantation energy of $E_{opt} = 5.2$ keV. The result also shows that a greater moderator efficiency can be achieved by collecting positrons that are emitted from the front surface. However, this requires a positron source which produces very low energy positrons. Also, a device that extracts the positrons from the front surface of the moderator is more complex than one that extracts positrons from the rear surface.

4.2.3 Measurement of positron annihilation in the moderator

VEP annihilation measurements were performed on moderators W2022A and W2022B. The moderators were placed between the primary grid G_1 and the secondary grid G_2 inside the vacuum chamber of the VEP facility. For these measurements, G_1 was charged with voltages of +30.0 and -30.0 V and G_2 was charged with a voltage of $V_{G2} = -30.0$ V. The positron beam acceleration energy E_a was varied from 0.1 to 18.3 keV $\pm 1\%$. For each measurement point, the HPGe detector registered the 511 keV peak count rate R_A for a time of 1700 s with dead time compensation. The peak count rate versus the positron beam acceleration energy of moderator W2022A after annealing at $T = 1102 \pm 10$ °C is shown in Figure 42.

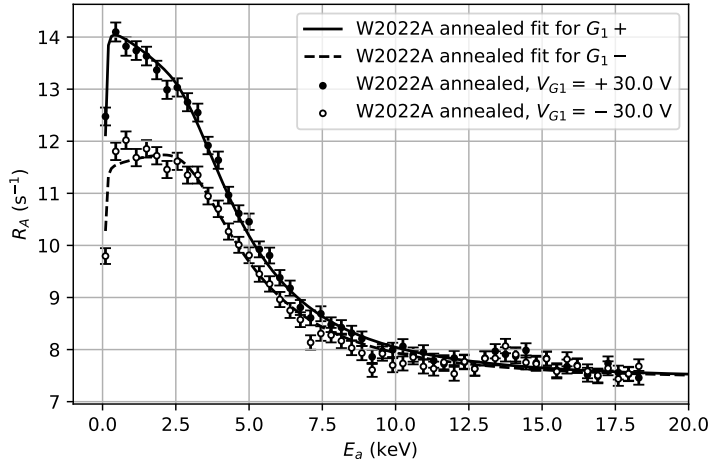


Figure 42: The measured 511 keV peak count rate R_A versus the positron beam acceleration energy E_a of moderator W2022A after it was annealed. This measurement was run with a positively and negatively charged primary grid G_1 . The indicated count rate error equals the 2σ standard deviation.

This result shows a clear difference in R_a between a positively and negatively charged grid G_1 . The result therefore proves that there is free positron emission from the front surface with a kinetic energy that is lower than 30.0 eV. The data points have some resemblance to the expected curves from the simulation that is shown in Figure 39. However, the simulation suggests that the count rate must go to zero at higher implantation energies, which is not the case in this measurement. Furthermore, the data shows that the foil could be thinner than expected or that the Makhov parameters are incorrect.

In order to fit the data, it was assumed that thickness of the tungsten foil equals 50 nm and that the Makhov parameters from Table 2 are incorrect for thin foils. Only α , n , ϵ_{e+} , the multiplier and the offset were needed as fit parameters. The surface branching ratios ϵ_{sb} and ϵ_{Ps} were both defined to be equal to $(1 - \epsilon_{e+})/2$. All other parameters are imposed according to Table 2. The fit parameters are shown in Table 3.

Table 3: Fit parameters for the annihilation measurement of moderator W2022A. The error equals the 1σ standard deviation.

ϵ_{e+}	0.39 ± 0.01	—
n	1.26 ± 0.01	—
α	12.9 ± 0.2	$\mu\text{g} \cdot \text{cm}^{-2} \cdot \text{keV}^{-1.26 \pm 0.01}$
Multiplier	6.8 ± 0.1	s^{-1}
Offset	7.41 ± 0.03	s^{-1}

The offset could have been caused by annihilation inside the molybdenum grid ring. Therefore, a positron annihilation measurement was performed on a grid ring without foil. For this measurement, E_a was varied from 0.1 to 24.9 keV $\pm 1\%$ and the measurement time per data point was 2000 s with dead time compensation. G_1 was charged with a voltage of $V_{G1} = -30.0$ V and G_2 was not installed. R_A versus E_a for a molybdenum grid ring without moderator is shown in Figure 43.

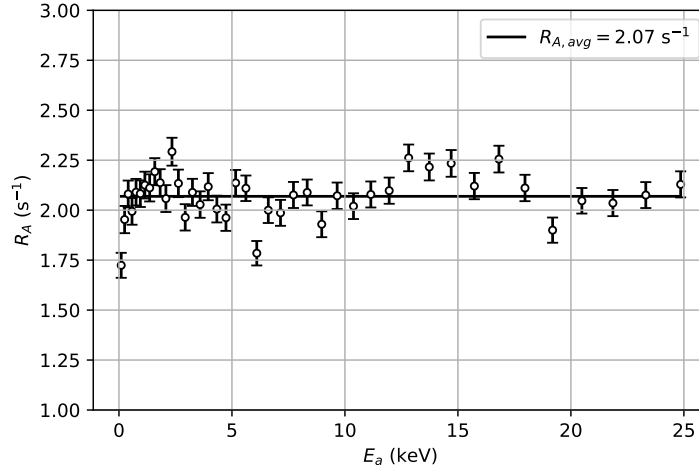


Figure 43: The measured 511 keV peak count rate R_a versus the positron beam acceleration energy E_a of a molybdenum grid ring without moderator. This measurement was run with a negatively charged primary grid G_1 . The average count rate is shown by the horizontal line that equals $R_{A,avg} = 2.07 \text{ s}^{-1}$. The indicated count rate error equals the 2σ standard deviation.

The average count rate, shown by the horizontal line, suggests a background count rate of $R_b = 2.07 \text{ s}^{-1}$ ($\sigma_{SD} = 0.12 \text{ s}^{-1}$). The offset count rate shown in Figure 42 equals 7.41 s^{-1} ($\sigma_{SD} = 0.03 \text{ s}^{-1}$). This shows that the molybdenum grid ring only causes a part of the background radiation that is observed in the positron annihilation measurement of moderator W2022A. It is expected that the other part of the background radiation could be caused by transmitted positrons which reflect from the beam dump back into the moderator. New experiments are needed to confirm this.

For moderator W2022B, a positron annihilation measurement was performed before and after the annealing process. The same settings were used as for the measurement of moderator W2022A. R_A versus E_a for a moderator W2022B as it was received before annealing, is shown in Figure 44.

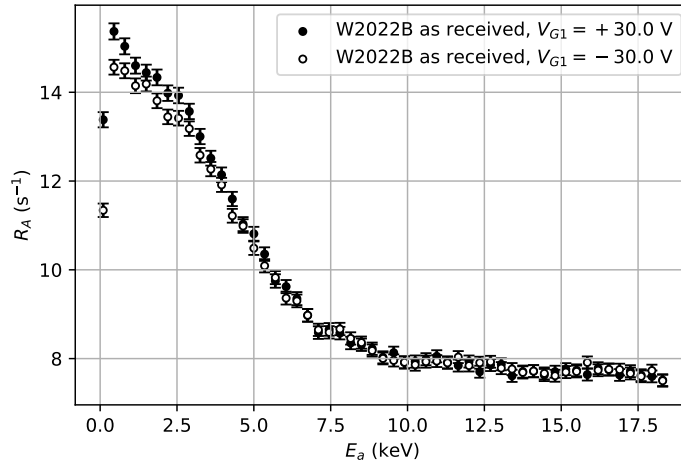


Figure 44: The measured 511 keV peak count rate R_a versus the positron beam acceleration energy E_a of moderator W2022B before it was annealed. This measurement was run with a positively and negatively charged primary grid G_1 . The indicated count rate error equals the 2σ standard deviation.

R_A versus E_a for a moderator W2022B after annealing at $T = 1094 \pm 10 \text{ }^\circ\text{C}$ is shown in Figure 45.

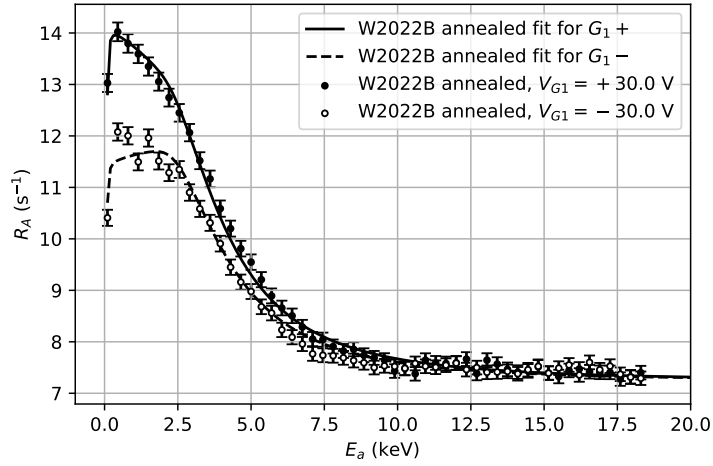


Figure 45: The measured 511 keV peak count rate R_a versus the positron beam acceleration energy E_a of moderator W2022B after it was annealed. This measurement was run with a positively and negatively charged primary grid G_1 . The indicated count rate error equals the 2σ standard deviation.

The results show that the annealing process increased the free positron emission fraction, thus ϵ_{fe+} must be increased. Also, the annihilation rate after annealing is lower, which suggests that more positrons could be emitted from the rear surface of the moderator or there is more positron reflection or more epithermal emission. Moderator W2022B seems to have a similar background count rate as W2022A. Furthermore, the background count rate of moderator W2022B is slightly reduced after annealing.

The same method to fit the annihilation measurement of moderator W2022A was used for W2022B. The fit parameters that were found are shown in Table 4.

Table 4: Fit parameters for the annihilation measurement of moderator W2022B. The error equals the 1σ standard deviation.

ϵ_{e+}	0.38 ± 0.01	—
n	1.26 ± 0.01	—
α	15.8 ± 0.3	$\mu\text{g} \cdot \text{cm}^{-2} \cdot \text{keV}^{-1.26 \pm 0.01}$
Multiplier	6.9 ± 0.1	s^{-1}
Offset	7.24 ± 0.02	s^{-1}

4.2.4 Measurement of positron transmission through the moderator

The transmission of positrons through moderator W2022A was measured using a HPGe detector. The VEP facility was extended with a straight beam tube to guide the transmitted positrons away from the moderator. A view port was mounted at the end of the tube which acts as a beam dump. The HPGe detector was positioned as close as possible to the view port to detect the annihilation radiation of the transmitted positrons. The measured 511 keV peak count rate of the transmitted positrons R_T versus the positron beam acceleration energy E_a is shown in Figure 46.

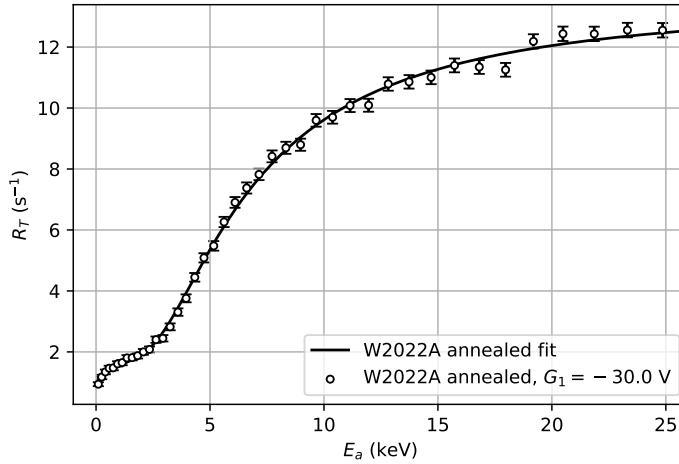


Figure 46: The count rate of positrons that are transmitted through moderator W2022A R_T versus the positron beam acceleration energy E_a . The indicated count rate error equals the 3σ standard deviation.

For acceleration energies lower than 3 keV, the result shows a non-horizontal line with a positive slope. This means that the effective diffusion length L_+ is in the order or greater than the thickness of the tungsten foil. Moreover, ϵ_{e+} is non-zero. Otherwise, the curve should look like the G_2+ line in Figure 40.

The transmission curve is fitted with the thin foil model with ϵ_{e+} , n , α , multiplier and offset as fit parameters. The surface branching ratios ϵ_{sb} and ϵ_{Ps} where both defined to be equal to $(1 - \epsilon_{e+})/2$. All other parameters are imposed according to Table 2. The fit parameters are shown in Table 5.

Table 5: Fit parameters for the transmission measurement of moderator W2022A. The error equals the 1σ standard deviation.

ϵ_{e+}	0.18 ± 0.05	—
n	0.79 ± 0.04	—
α	21.0 ± 1.7	$\mu\text{g} \cdot \text{cm}^{-2} \cdot \text{keV}^{-0.79 \pm 0.04}$
Multiplier	12.5 ± 0.2	s^{-1}
Offset	1.1 ± 0.1	s^{-1}

The fit parameters ϵ_{e+} , n and α that are found with the transmission measurement of moderator W2022A differ from the ones that are found with the annihilation measurement. This demonstrates that the characterization parameters are not as accurately extracted as the standard deviation error may suggest.

Further development of the annihilation and transmission measurements and the thin foil model is needed in order to obtain accurate characterization parameters. Two problems that should be solved in future experiments are:

- The annihilation measurements show a higher-than-expected background count rate. Therefore, the transmission measurement could be missing counts by positrons that reflect from the beam dump back into the moderator. How can the offset count rate be explained?
- The thin foil model cannot be fitted on the measured data without changing the Makhov parameters or foil thickness. How can the positron implantation curves be parameterized for thin foils?

The effect of a secondary retarding field grid

A retarding field experiment was conducted to prove that the tungsten foil moderators emit thermalized positrons from the rear surface. Therefore, the secondary grid G_2 was installed behind moderator W2022A. This grid was connected to a computer-controlled voltage source of the VEP facility. The voltage was varied from 0.00 to 9.96 V ± 0.01 V. The VEP facility was configured to deliver a $E_a = 3.4 \pm 1\%$ keV positron beam onto the moderator. The positrons that are emitted by the moderator are detected by the MCP if their kinetic energy is great enough to pass the potential barrier of G_2 . The voltage of G_1 was configured at +30.0 V. For each data point, the voltage of G_2 was fixed and the count rate R_{MCP} was measured for time of 100 s with dead time compensation.

The result of this experiment reassembles the shape of the error function. Therefore, it could be parameterized by:

$$R_{fit}(V_{G2}) = a\sigma\sqrt{\frac{\pi}{2}}\operatorname{erf}\left(\frac{V_{G2} - \mu}{\sigma_V\sqrt{2}}\right) + b. \quad (46)$$

The derivative of this function is similar as Equation 45.

R_{MCP} versus the retarding field potential V_{G2} including a fit with Equation 46 is shown in Figure 47.

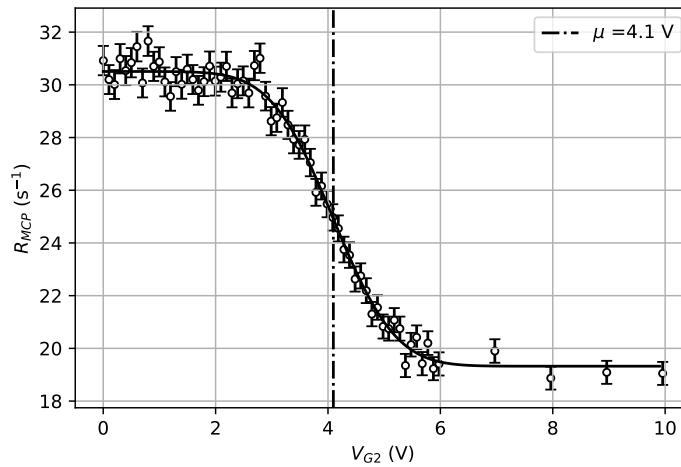


Figure 47: The count rate of the MCP detector R_{MCP} versus the secondary grid voltage V_{G2} . The MCP detector measures the emitted positrons from the rear side of moderator W2022A. Each point has a measurement time of 100 s with dead time compensation. The acceleration energy was set on $E_a = 3.4 \pm 1\%$ keV. The data was fitted using Equation 46 where $a = -5.1 \text{ s}^{-1} \cdot \text{V}^{-1}$, $\mu = 4.1 \text{ V}$, $b = 25 \text{ s}^{-1}$ and $\sigma_V = 0.87 \text{ V}$. The indicated count rate error equals the 1σ standard deviation.

The result shows that moderator W2022A emits thermalized positrons, because positrons are emitted with a mean energy of 4.1 eV, which is within same order of magnitude as the work function ϕ_+ . However, the mean energy should not be considered as a measurement of ϕ_+ , because it is a combination of the work functions of the moderator and the retarding field grid. The MCP detector gives a background count rate by voltages over 6 V, which is mainly caused by dark counts and positrons that pass through small holes in the moderator.

The parameters $a = -5.1 \text{ s}^{-1} \cdot \text{V}^{-1}$, $\mu = 4.1 \text{ V}$, $b = 25 \text{ s}^{-1}$ and $\sigma_V = 0.87 \text{ V}$ were found as a result of fitting Equation 46 onto R_{MCP} . With these parameters, an energy spectrum of the emitted thermalized positrons can be parameterized using Equation 45. This energy spectrum is shown in Figure 48.

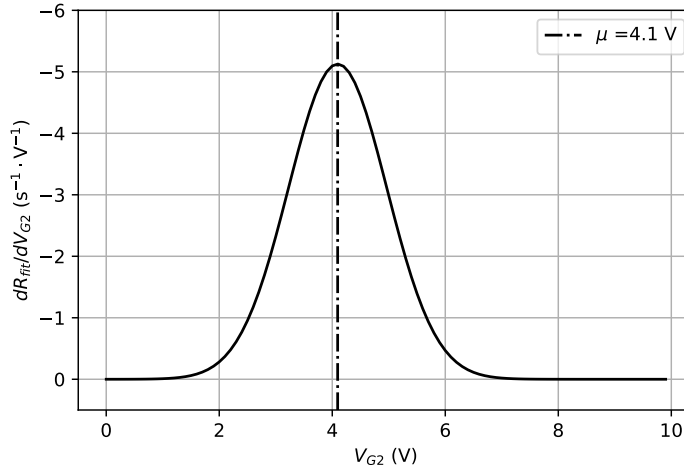


Figure 48: A Gaussian parameterization of the expected energy spectrum of thermalized positrons that are emitted by moderator W2022A.

The monoenergeticity of the moderated positrons in W2022A is given by the variance of Gaussian curve which equals $\sigma_E = 0.87$ eV. Not all positrons incident on the moderator will be thermalized, therefore an energy filter is required to obtain a pure monoenergetic beam.

Moderator efficiency

VEP transmission measurements were performed on the moderators with a secondary grid voltages V_{G2} of +30.0 and -30.0 V. The primary grid voltage V_{G1} was fixed to +30.0 V. According to Equation 41, the count rate difference for both voltages on G_2 divided by the count rate of the incident positron beam equals the rear surface emitted thermalized positron fraction F_{re+} . The maximum measured value of F_{re+} equals the moderator efficiency η . Fraction F_{re+} of the moderator W2022A was measured after annealing, for a period of 250 s per data point. For verification, a second measurement was performed during a period of 500 s per data point. This data was fitted with the thin foil model. Both measurements of F_{re+} versus the acceleration energy E_a are shown in Figure 49.

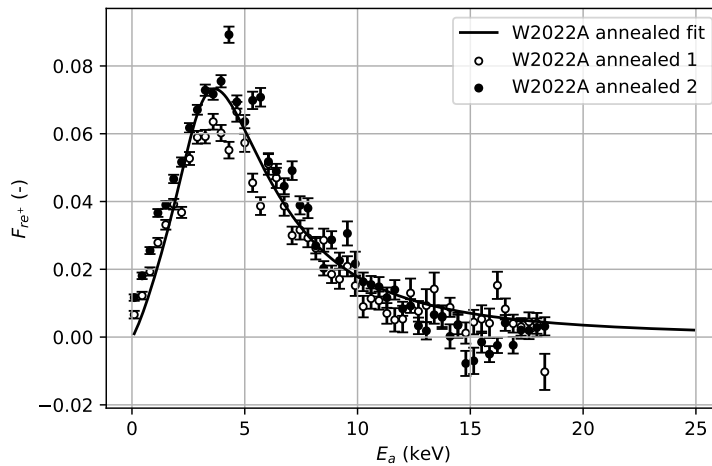


Figure 49: The emitted thermalized positron fraction from the rear surface F_{re+} of moderator W2022A versus the acceleration energy E_a . The indicated count rate error equals the 1σ standard deviation.

The result shows that the optimal implantation energy is lower than the expected value of 5.2 keV. This was calculated using the thin foil model as is shown in Figure 41. A reason for the difference could be that the moderator is thinner than 50 nm. The implantation model could also be inaccurate for thin

foils. This problem was resolved in the same way as for the annihilation and transmission measurements. Therefore, it was assumed that the implantation model is incorrect, and that thickness of moderator foils is exactly 50 nm.

The thin foil model was used to fit the data shown in Figure 49 by changing ϵ_{e^+} and the Makhov parameters α and n . All other parameters are imposed and can be found in Table 2. The fit parameters, the optimum implantation energy E_{opt} and the moderator efficiency η can be found in Table 6.

Table 6: Characterization parameters of moderator W2022A found by the thin foil model. The errors were propagated from a 1σ standard deviation.

ϵ_{e^+}	0.175 ± 0.005	—
n	1.23 ± 0.04	—
α	11.4 ± 0.7	$\mu\text{g} \cdot \text{cm}^{-2} \cdot \text{keV}^{-1.23 \pm 0.04}$
E_{opt}	3.7 ± 0.1	keV
η	0.073 ± 0.002	—

The same measurement has been performed on moderator W2022B before and after annealing. This is shown in Figure 50.

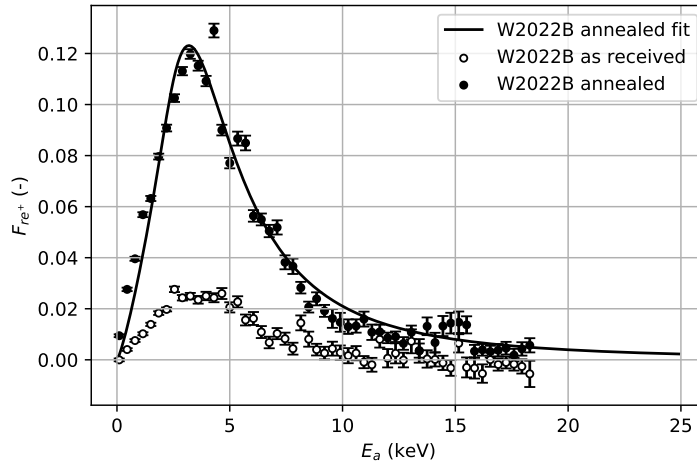


Figure 50: The emitted thermalized positron fraction from the rear surface F_{re^+} of moderator W2022B versus the acceleration energy E_a . The indicated count rate error equals the 1σ standard deviation.

This result shows a clear improvement in moderator efficiency after annealing. Furthermore, the efficiency of moderator W2022B is greater than W2022A. The curve of F_{re^+} from moderator W2022B after annealing is also fitted with the thin foil model to extract characterization parameters. These values are shown in Table 7.

Table 7: Characterization parameters of moderator W2022B found by the thin foil model. The errors were propagated from a 1σ standard deviation.

ϵ_{e^+}	0.294 ± 0.007	—
n	1.25 ± 0.04	—
α	13.2 ± 0.9	$\mu\text{g} \cdot \text{cm}^{-2} \cdot \text{keV}^{-1.25 \pm 0.04}$
E_{opt}	3.2 ± 0.1	keV
η	0.123 ± 0.002	—

The found values for ϵ_{e^+} in Table 6 and Table 7 are expected to be more accurate than the values that were found in the annihilation and transmission measurement, because the other positron branching ratios ϵ_{sb} and ϵ_{Ps} do not have to be known in order to fit the results shown in Figure 49 and Figure 50. Additionally, the annihilation measurement has background counts which could not be explained. The

transmission measurement may be affected by this problem as well. Furthermore, the difference found in the values for ϵ_{e^+} in Table 6 and Table 7 correspond with the difference between the efficiencies of moderator W2022A and W2022B. It can therefore be concluded that ϵ_{e^+} of moderator W2022A equals $\epsilon_{e^+} = 0.175 \pm 0.005$ and for moderator W2022B equals $\epsilon_{e^+} = 0.294 \pm 0.007$.

4.3 Intense Positron Beam lifetime spectrometer

This section includes the results from the:

- Beam alignment,
- Positron lifetime spectrum measurement.

4.3.1 Beam alignment

The positron beam was aligned by trial and error with the help of the MCP with the fluorescent screen. In Figure 51, a time integrated image of the positron beam at the sample location is shown.

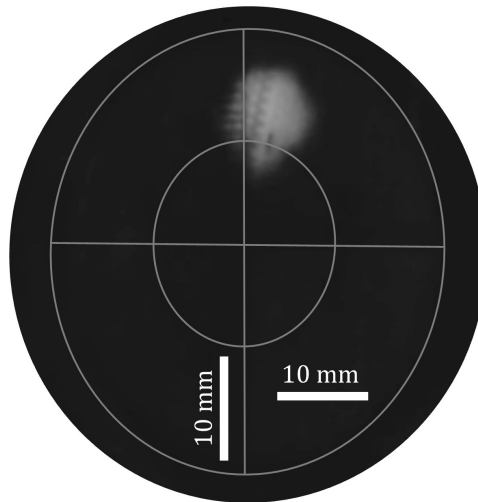


Figure 51: The positron beam profile and position detected by a MCP with a fluorescent screen. The image is not round because the photograph was taken at an angle. Therefore, the vertical and horizontal indicator do not have the same length.

This result shows that the positrons reach the MCP with the fluorescent screen. Additionally, it shows that the beam has a slight diamond shaped profile, which implies that the beam must have traveled through the carbon foil, as it is the only component with a diamond shaped opening. Additionally, the image shows that the positron beam is not on center within the vacuum chamber. Unsuccessful attempts have been made to center the beam. For producing this image, the POSH-PALS facility was configured with the settings shown in Table 8.

Table 8: The settings that were found to align the positron beam of the POSH-PALS facility.

Magnetic correction coils cage	Front-back	+2.17 A
	Left-right	+0.34 A
	Top-bottom	+0.68 A
Magnetic guidance	Coils 02,03,04	+1.05 A
Magnetic correction before B-E converter	Vertical	0.00 A
	Horizontal	-1.2 A
Magnetic correction after B-E converter	Vertical	0.00 A
	Horizontal	0.00 A
B-E converter	V_1	-6.0 kV
	V_3	+0.9 kV
	V_4	-5.0 kV
	V_5	-1.75 kV
Photo multiplier tube	V_{PMT}	-2.05 kV
Electron MCP	Front	-1.90 kV
	Back	GND
	Anode	+0.60 kV
Voltage vacuum chamber (New ground)	V_N	-3.5 kV
Grid and MCP voltages on new ground	Moderator (V_T)	+0.65 kV
	Focus grid before mirror	-0.40 kV
	Mirror	+0.65 kV
	Carbon foil	-6.2 kV
	Grid after carbon foil	-0.69 kV
	Positron MCP front	-1.86 kV
	Grid before positron MCP	-0.70 kV
	Positron MCP screen	+2.75 kV

Secondary electrons were detected with the MCP detector while the POSH-PALS facility was configured with the settings shown in Table 8. Only when beam tube was opened, a count rate of more than 10^4 s^{-1} was observed. The potential of the front of this MCP (-1.90 kV) was set higher than the potential of the positrons ($V_N + V_T = -2.85 \text{ kV}$). Therefore, the possibility that a positron was detected as an electron was eliminated.

4.3.2 Positron lifetime spectrum measurement

Once the positron beam was aligned with the settings shown in Table 8, a lifetime spectrum could be measured. The goal was to aim the positron beam at the MCP with the fluorescent screen and measure its lifetime spectrum. It could not be prevented that positrons annihilate in other parts inside the vacuum chamber. This adds other exponential decay components onto the lifetime spectrum.

The PC connected to the ADC was configured to measure for a period of 40 hours. The TAC was calibrated using Ortec 462 Time Calibrator. Both the calibrator and the TAC have a reported time accuracy of ± 10 ps [16] [17]. The TAC was configured to the shortest range in time of 50 ns. The measured lifetime spectrum of the POSH-PALS facility for a transport energy of $E_T = 0.65$ keV is shown in Figure 52.

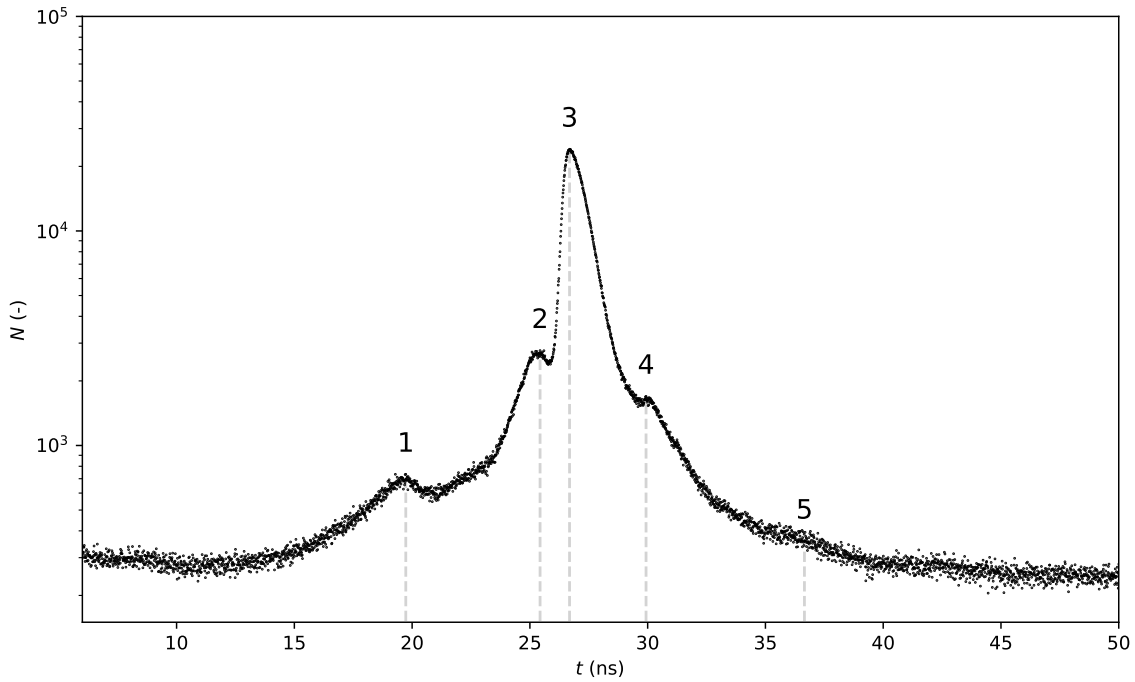


Figure 52: A positron lifetime spectrum measured using the POSH-PALS facility for a transport energy of $E_T = 0.65$ keV. This histogram shows the number of the detections N versus the positron lifetime t . All significant peaks are indicated with a number.

This result shows multiple peaks of different intensities. The peak in the middle at $t_{p3} = 26.7$ ns shows the characteristic shape of exponential decay convolved with a Gaussian function. Therefore, it is a positron lifetime spectrum. It is very unlikely that other processes within the POSH-PALS facility can produce similar results. The positions in time of all peaks are shown in Table 9.

Table 9: The position in time of the peaks shown in the positron lifetime spectrum.

$$\begin{aligned} t_{p1} &= 19.7 \text{ ns} \\ t_{p2} &= 25.4 \text{ ns} \\ t_{p3} &= 26.7 \text{ ns} \\ t_{p4} &= 29.9 \text{ ns} \\ t_{p5} &= 36.7 \text{ ns} \end{aligned}$$

To extract the time resolution, the peak at $t = t_{p3}$ is fitted with Equation 39 for a single Gaussian time resolution function f_σ and lifetime τ . This is shown in Figure 53.

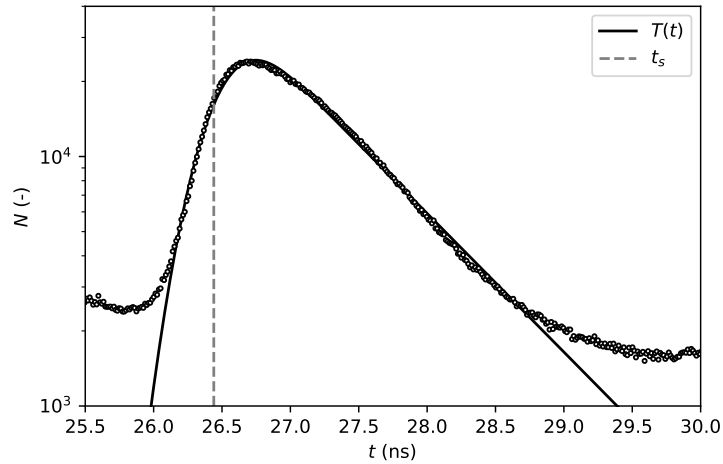


Figure 53: The measured positron lifetime spectrum using the POSH-PALS facility fitted with the positron lifetime model. This histogram shows the number of the detections N versus the positron lifetime t . The fit parameters are $\sigma_t = 0.24$ ns, $\tau = 0.78$ ns and $t_s = 26.4$ ns.

This indicates that the time resolution function has a variance σ_t of 0.24 ns. This equals a FWHM of 0.57 ns. The other fit parameters are $\tau = 0.78$ ns and $t_s = 26.4$ ns.

The result in Figure 52 shows a lifetime spectrum. However, too many signals are mixed to be able to extract multiple positron lifetimes. Further development of the POSH-PALS facility is needed to remove unwanted peaks from the lifetime spectrum and to improve its time resolution. It is expected that the multiple peaks probably arise by positrons that do not annihilate at the intended sample location. These peaks can also be caused by an electrical problem. For example, by electrical reflections or the SCA could occasionally trigger incorrectly. An electrical problem can be ruled out in later experiments by changing the transport energy of the positrons. This alters the time of flight of the positrons, which could reposition the peaks in the time spectrum.

A manual fit has been made to show that the full lifetime time spectrum can be composed of multiple decay peaks with positive and negative lifetimes. Each peak is described by Equation 39 for a single positron lifetime τ . In Figure 54, the manually fitted curve T_{sum} is shown on top of the measured lifetime spectrum.

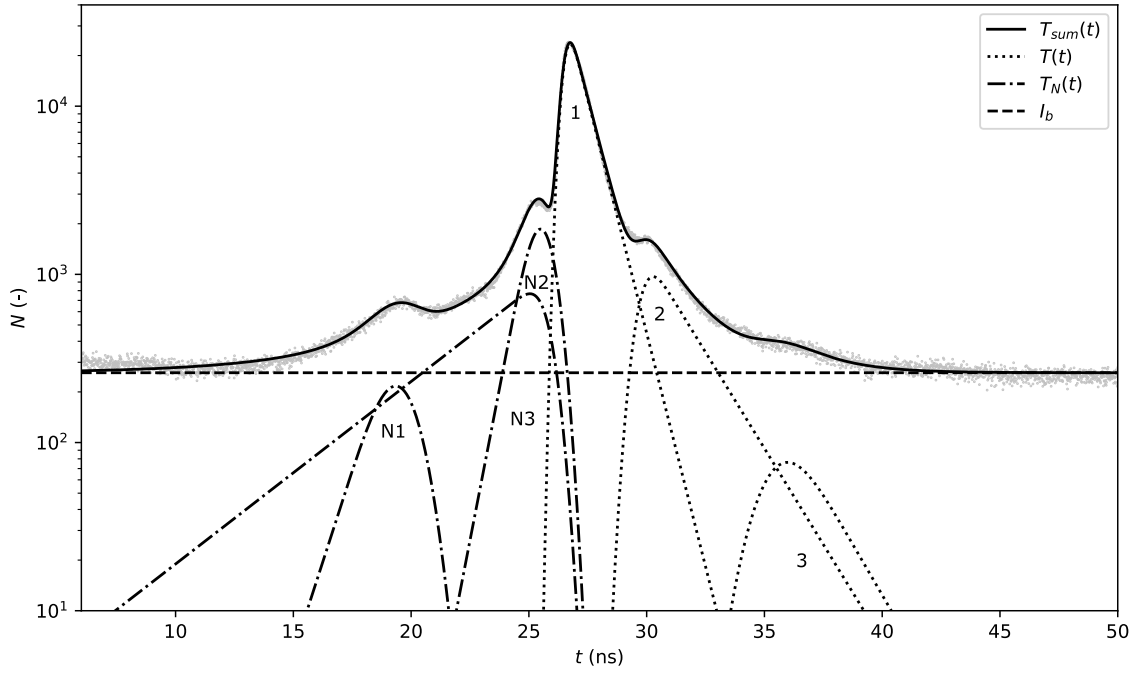


Figure 54: The measured positron lifetime spectrum which is manually fitted by a sum of multiple decay peaks $T_{sum}(t)$.

The background intensity I_b has a value of 260 and all other fit parameters that were found are shown in Table 10.

Table 10: The manually found fit parameters to describe the curve of the measured positron lifetime spectrum.

	σ_t (ns)	τ (ns)	t_s (ns)	I (-)
$T_1(t)$	0.24	0.78	26.4	40000
$T_2(t)$	0.45	1.90	29.6	1500
$T_3(t)$	1.00	1.80	35.0	170
$T_{N1}(t)$	0.80	-1.00	20.0	600
$T_{N2}(t)$	0.50	-0.60	25.9	5300
$T_{N3}(t)$	0.50	-4.00	25.9	1000

The positron lifetime spectrum seems to have peaks with a negative τ . It could be caused by an electrical problem with the TAC. It is observed that the count rate of MCP detector is at least an order of magnitude greater than the count rate of scintillation detector. Therefore, the TAC receives more start than stop pulses. Also, each positron could generate multiple secondary electrons which can possibly hit the MCP detector at different points in time. Further research is needed to find out if why these peaks seem to have a negative τ .

5 Conclusion

The POSH-PALS facility has been brought into a further and new stage of its development, as it is now able to measure a positron lifetime spectrum. This lifetime spectrum is still rather crude as it shows multiple peaks and it has a time resolution function with a variance σ_t of 0.24 ns. This equals a FWHM of 0.57 ns. As a result, multiple positron lifetimes could not be resolved.

The positron beam within the POSH-PALS facility has been aligned such that it travels through the carbon foil and ends up into the MCP with screen. The moderator characterization experiments have showed that both moderators can emit thermalized positrons. Moderator W2022A has a measured efficiency of $\eta = 0.073 \pm 0.002$ when the positron implantation energy equals $E_{opt} = 3.7 \pm 0.1$ keV and a positron emission branching ratio of $\epsilon_{e^+} = 0.175 \pm 0.005$. Moderator W2022B has a measured efficiency of $\eta = 0.123 \pm 0.002$ when the positron implantation energy equals $E_{opt} = 3.2 \pm 0.1$ keV and a positron emission branching ratio of $\epsilon_{e^+} = 0.294 \pm 0.007$.

Acknowledgements

I thank Dr. H. Schut and Ing. M.R. de Boer for giving me the opportunity to work with them on developing the POSH-PALS facility. Their collaboration was essential for achieving the research goal. Therefore, they deserve credit for all measurement results shown in this thesis report. I would also like to thank Dr. M. Butterling who was responsible for designing and building the POSH-PALS facility.

References

- [1] H. Schut. “Development of an Intense Positron Beam lifetime spectrometer (POSH-PALS),” [Online]. Available: <https://www.tudelft.nl/en/faculty-of-applied-sciences/about-faculty/departments/radiation-science-technology/research/research-groups/neutron-positron-methods-for-materials/education/student-projects>.
- [2] R. Krause-Rehberg. “Positronannihilation.net.” Accessed: 6 March 2022, [Online]. Available: <http://www.positronannihilation.net>.
- [3] A. van Veen, H. Schut, F. Labohm, and J. de Roode, “Positron extraction and transport in a nuclear-reactor-based positron beam,” *Nuclear Instruments and Methods in Physics Research Section A: Accelerators, Spectrometers, Detectors and Associated Equipment*, vol. 427, no. 1, pp. 266–270, 1999.
- [4] W. Egger, *PLEPS: Pulsed low energy positron system*. Aug. 2015.
- [5] “Positron Annihilation Spectroscopy at the HZDR.” Accessed: 6 March 2022, [Online]. Available: <https://www.hzdr.de/db/Cms?pNid=3581>.
- [6] H. Schut, *A Variable Positron Beam Facility with Applications in Materials Science*. 1990.
- [7] ———, *Lecture about Positron Annihilation techniques for material defect studies*. Faculty of Applied Sciences, Delft University of Technology, Oct. 2021.
- [8] W. Brandt, I. S. of Physics “Enrico Fermi.”, S. italiana di fisica, and A. Dupasquier, *Positron Solid-state Physics: Varenna on Lake Como, Villa Monastero, 14-24 July 1981*, ser. Enrico Fermi International School of Physics Series v. 83. North-Holland Publishing Company, 1983.
- [9] P. J. Schultz and K. G. Lynn, “Interaction of positron beams with surfaces, thin films, and interfaces,” *Rev. Mod. Phys.*, vol. 60, pp. 701–779, 3 Jul. 1988.
- [10] A. P. Mills and R. J. Wilson, “Transmission of 1 - 6-keV positrons through thin metal films,” *Phys. Rev. A*, vol. 26, pp. 490–500, 1 Jul. 1982.
- [11] S. Valkealahti and R. Nieminen, “Monte Carlo calculations of keV electron and positron slowing down in solids. II,” *Applied Physics A*, vol. 35, no. 1, pp. 51–59, 1984.
- [12] A. Vehanen, K. Saarinen, P. Hautojärvi, and H. Huomo, “Profiling multilayer structures with monoenergetic positrons,” *Phys. Rev. B*, vol. 35, pp. 4606–4610, 10 Apr. 1987.
- [13] D. T. Britton, P. C. Rice-Evans, and J. H. Evans, “Epithermal effects in positron depth profiling measurements,” *Philosophical Magazine Letters*, vol. 57, no. 3, pp. 165–169, 1988.
- [14] J. Shultis and R. Faw, *Fundamentals of Nuclear Science and Engineering*. CRC Press, 2017.
- [15] A. Vehanen, K. Lynn, P. J. Schultz, and M. Eldrup, “Improved slow-positron yield using a single crystal tungsten moderator,” *Applied Physics A*, vol. 32, no. 3, pp. 163–167, 1983.
- [16] ORTEC, *Model 462 Time Calibrator Operating and Service Manual*, English, 2007, 10 pp.
- [17] ———, *Model 566 Time-to-Amplitude Converter (TAC) Operating and Service Manual*, English, 2011, 16 pp.

Appendices

A Derivation of the Green's function of the positron transport equation

Starting with the one-dimensional steady-state transport equation for thermalized positrons:

$$D_+ \frac{d^2 c(z)}{dz^2} - \frac{d(v_d(z)c(z))}{dz} - (\nu_t n_t(z) + \lambda_b)c(z) + I(z) = 0. \quad (47)$$

The homogeneous Dirichlet boundary conditions for a foil with thickness L :

$$c(0) = c(L) = 0. \quad (48)$$

It is assumed that there is not electric field within the foil:

$$v_d = \mu E = 0. \quad (49)$$

The equation can now be reduced to:

$$D_+ \frac{d^2 c(z)}{dz^2} - Ac(z) = -I(z) \quad 0 \leq z \leq L, \quad (50)$$

where:

$$A = \nu_t n_t + \lambda_b. \quad (51)$$

Direct method

The following equivalent problem is used for finding the Green's function with the direct method:

$$\frac{d^2 G(z; z_0)}{dz^2} - \alpha^2 G(z; z_0) = -\frac{\delta(z - z_0)}{D_+} \quad 0 \leq z \leq L, \quad (52)$$

where:

$$\alpha = \sqrt{\frac{A}{D_+}}. \quad (53)$$

The same homogeneous Dirichlet boundary conditions hold for $G(z; z_0)$:

$$G(0; z_0) = G(L; z_0) = 0. \quad (54)$$

The value of α is always positive, therefore the solution of $G(z; z_0)$ equals

$$G(z; z_0) = \begin{cases} c_1 \sinh(\alpha z) + c_2 \cosh(\alpha z) & \text{for } 0 \leq z < z_0 \\ c_3 \sinh(\alpha(z - L)) + c_4 \cosh(\alpha(z - L)) & \text{for } 0 < z \leq L \end{cases}. \quad (55)$$

Applying the boundary conditions leads to:

$$G(0; z_0) = c_2 = 0, \quad (56)$$

$$G(L; z_0) = c_4 = 0. \quad (57)$$

The solution $G(z; z_0)$ must be continuous, therefore:

$$G(z_0^-; z_0) = G(z_0^+; z_0). \quad (58)$$

This results in the following relation:

$$c_1 \sinh(\alpha z_0) - c_3 \sinh(\alpha(z_0 - L)) = 0. \quad (59)$$

The solution must also satisfy the integral condition:

$$\int_{z_0^-}^{z_0^+} \frac{d^2 G(z; z_0)}{dz^2} dz - \int_{z_0^-}^{z_0^+} \alpha^2 G(z; z_0) dz = - \int_{z_0^-}^{z_0^+} \frac{\delta(z - z_0)}{D_+} dz = \frac{-1}{D_+} \quad (60)$$

Due to $G(z; z_0)$ being continuous, the second integral must be zero:

$$\int_{z_0^-}^{z_0^+} \alpha^2 G(z; z_0) dz = 0. \quad (61)$$

The integral condition can now be simplified to:

$$\left[\frac{dG(z; z_0)}{dz} dz \right]_{z_0^-}^{z_0^+} = \frac{-1}{D_+}. \quad (62)$$

This gives following relation:

$$-c_1 \alpha \cosh(\alpha z_0) + c_3 \alpha \sinh(\alpha(z_0 - L)) = \frac{1}{D_+}. \quad (63)$$

The two relations can be written in a matrix-vector equation:

$$\begin{bmatrix} \sinh(\alpha z_0) & -\sinh(\alpha(z_0 - L)) \\ -\alpha \cosh(\alpha z_0) & \alpha \sinh(\alpha(z_0 - L)) \end{bmatrix} \begin{bmatrix} c_1 \\ c_3 \end{bmatrix} = \begin{bmatrix} 0 \\ 1/D_+ \end{bmatrix}. \quad (64)$$

The constants can be found by inverting the matrix:

$$\frac{1}{\alpha \sinh(\alpha L)} \begin{bmatrix} \alpha \sinh(\alpha(z_0 - L)) & \sinh(\alpha(z_0 - L)) \\ \alpha \cosh(\alpha z_0) & \sinh(\alpha z_0) \end{bmatrix} \begin{bmatrix} 0 \\ 1/D_+ \end{bmatrix} = \begin{bmatrix} c_1 \\ c_3 \end{bmatrix}, \quad (65)$$

$$\begin{bmatrix} c_1 \\ c_3 \end{bmatrix} = \begin{bmatrix} \sinh(\alpha(z_0 - L))/(D_+ \alpha \sinh(\alpha L)) \\ \sinh(\alpha z_0)/(D_+ \alpha \sinh(\alpha L)) \end{bmatrix}, \quad (66)$$

All constants are now known and therefore, the solution can be fully written out:

$$G(z; z_0) = \begin{cases} \frac{\sinh(\alpha(z_0 - L)) \sinh(\alpha z)}{\beta \sinh(\alpha L)} & \text{for } 0 \leq z < z_0 \\ \frac{\sinh(\alpha(z - L)) \sinh(\alpha z_0)}{\beta \sinh(\alpha L)} & \text{for } z_0 < z \leq L \end{cases}, \quad (67)$$

where:

$$\alpha = \sqrt{\frac{A}{D_+}} = \sqrt{\frac{\nu_t n_t + \lambda_b}{D_+}}, \quad (68)$$

$$\beta = \alpha D_+ = \sqrt{D_+ (\nu_t n_t + \lambda_b)}. \quad (69)$$

The function $G(z; z_0)$ is plotted in Figure 55 for three different values for z_0 .

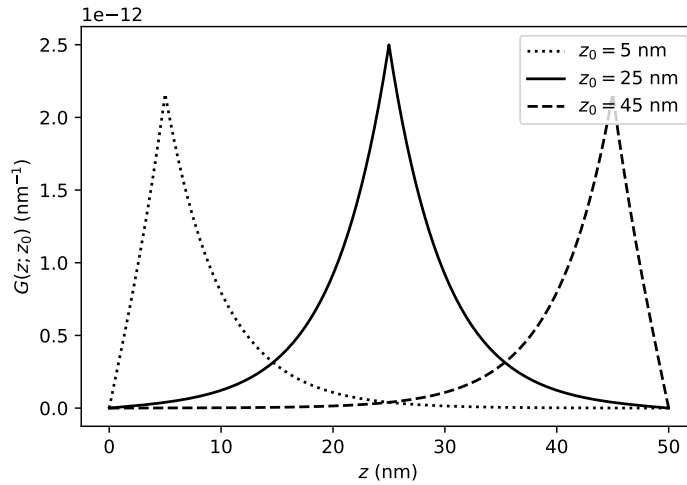


Figure 55: The Green's function of $c(z, E)$. For this example, the functions are plotted for $z_0 = 5, 25$ and 45 nm. The thickness L equals 50 nm and the diffusion length L_+ is set on 5 nm.

The function $G(z; z_0)$ is plotted in Figure 56 for three different diffusion lengths.

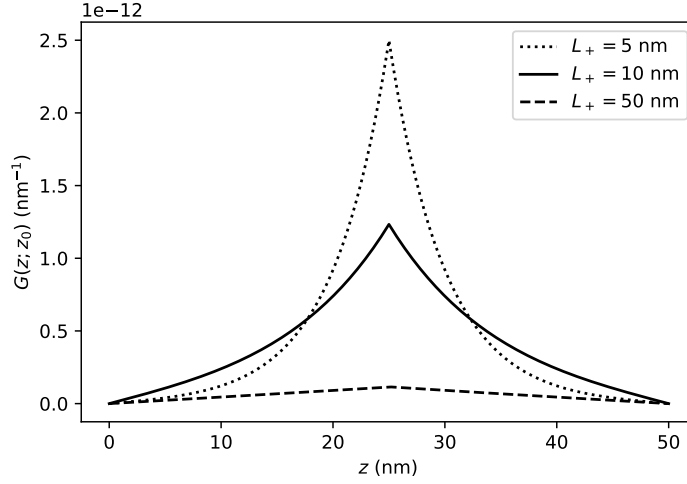


Figure 56: The Green's function of $c(z, E)$. For this example, the function is plotted for $z_0 = 5$ nm. The thickness L equals 50 nm and the diffusion length L_+ is shown for 5, 10 and 50 nm.

Eigenfunction expansion method

This method starts the reduced steady-state transport equation shown in Equation 50. The same boundary conditions hold as in Equation 48. The solution of $c(z)$ is defined as the following series:

$$c(z) = \sum_n a_n \varphi_n(z), \quad (70)$$

where a_n is a constant and $\varphi_n(z)$ is the eigenfunction. $\varphi_n(z)$ is solution of the following defined differential equation:

$$\frac{d^2 \varphi_n(z)}{dz^2} = -\lambda_n \varphi_n(z). \quad (71)$$

The same homogeneous Dirichlet boundary conditions as for $c(z)$ hold for $\varphi_n(z)$:

$$\varphi_n(0) = \varphi_n(L) = 0. \quad (72)$$

The solution of Equation 71 is shown below:

$$\varphi_n(z) = \sin(\sqrt{\lambda_n} z) = \sin\left(\frac{n\pi z}{L}\right) \quad \text{for } n = 1, 2, 3, \dots, \quad (73)$$

where λ_n is the eigenvalue. The solution shown Equation 70 can now be substituted into steady-state transport equation:

$$\sum_{n=1}^{\infty} [D_+ \lambda_n a_n \varphi_n(z) + A a_n \varphi_n(z)] = I(z), \quad (74)$$

$$\sum_{n=1}^{\infty} (D_+ \lambda_n + A) a_n \varphi_n(z) = I(z). \quad (75)$$

Since Equation 75 is a Fourier sine series, the coefficients are then given by:

$$(D_+ \lambda_n + A) a_n = \frac{2}{L} \int_0^L I(\bar{z}) \varphi_n(\bar{z}) d\bar{z}. \quad (76)$$

Isolation of a_n gives:

$$a_n = (D_+ \lambda_n + A)^{-1} \frac{2}{L} \int_0^L I(\bar{z}) \varphi_n(\bar{z}) d\bar{z}. \quad (77)$$

The full solution of $c(z)$ can now be written down:

$$c(z) = \int_0^L I(\bar{z}) \underbrace{\sum_{n=1}^{\infty} \sin\left(\frac{n\pi\bar{z}}{L}\right) \sin\left(\frac{n\pi z}{L}\right) \frac{2}{L} \left(\frac{\pi^2 n^2}{L^2} D_+ + A\right)^{-1}}_{G(z;\bar{z})} d\bar{z}. \quad (78)$$

Isolating the Green's function gives:

$$G(z; z_0) = \sum_{n=1}^{\infty} \frac{2 \sin\left(\frac{\pi n z_0}{L}\right) \sin\left(\frac{\pi n z}{L}\right)}{L \left(\frac{\pi^2 n^2}{L^2} D_+ + \nu_t n_t + \lambda_b\right)}. \quad (79)$$

The function $G(z; z_0)$ derived with the eigenfunction expansion method can be approximated by only calculating the first terms. The accuracy increases when more terms are calculated. This is shown in Figure 57 for the first 5, 10 and 1000 terms.

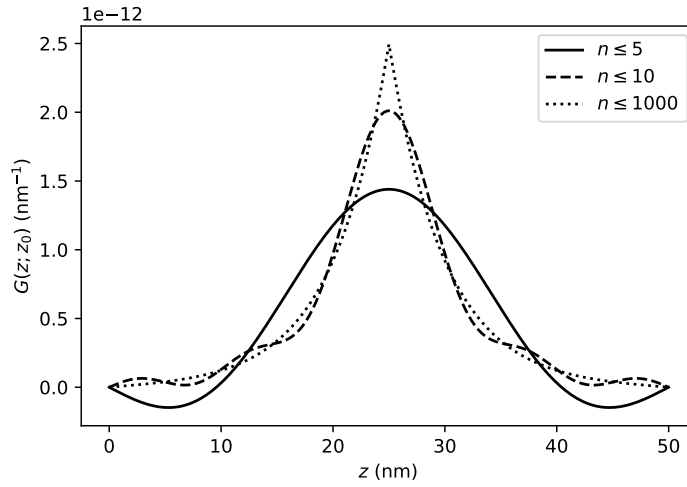


Figure 57: The Green's function of $c(z, E)$ derived with the eigenfunction expansion method with a finite number of 5, 10, and 1000 terms. For this example, the function is plotted for $z_0 = 5$ nm. The thickness L equals 50 nm and the diffusion length L_+ is shown for 5 nm.

A similar plot can like in Figure 55 can be made with the solution of $G(z; z_0)$ derived with the eigenfunction expansion method. In Figure 58, the solution of $G(z; z_0)$ is shown for $z_0 = 5, 25$ and 45 nm with only the first 10 terms.

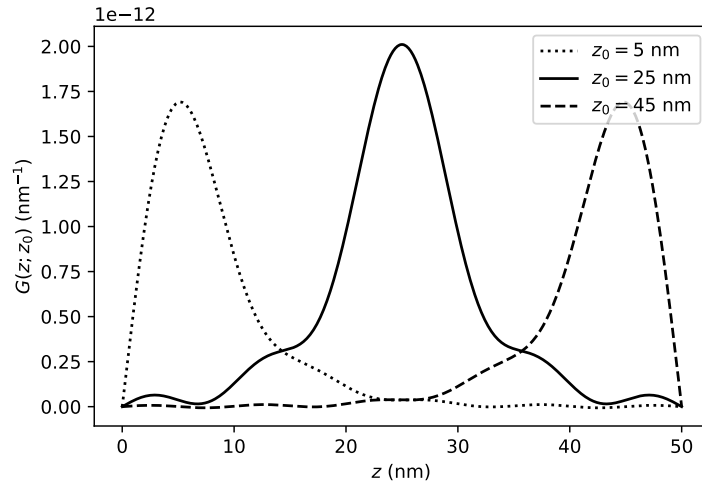


Figure 58: The Green's function of $c(z, E)$ derived with the eigenfunction expansion method with a finite number of 10 terms. For this example, the function is plotted for $z_0 = 5, 25$ and 45 nm. The thickness L equals 50 nm and the diffusion length L_+ is shown for 5 nm.

B Moderator foil handling

The moderator foils are delicate and cannot be touched by hand or instrument. Thin foils tend to stick to all solid objects if contact is made. Therefore, water is used to transfer the tungsten foil to its molybdenum grid.

A new moderator foil is delivered on a fine mesh which is glued on a glass plane. Between the mesh and the foil, there is a material that is soluble in water. This construction is slowly slid into the water via a ramp. The foil will separate from the mesh and will float purely on the water's surface tension. A photograph of this process with a 50 nm thick dummy foil is shown in Figure 59.



Figure 59: A photograph of a 50 nm thick tungsten dummy foil that is being separated from its glass plane with the help of water. Demineralized water is held by a square plastic container. The glass plane is slowly slid on a transparent plastic ramp into the water. The movement is guided with the help of tweezers. The right part of the foil is lifted up by the surface tension of the water. The other part of the foil sits on its mesh. A molybdenum grid ring held by a reversed action tweezers and is already put underwater.

It is possible that the tungsten foil is partly glued on the fine mesh. If that is the case, then the foil is not able to fully separate from the mesh unless those parts are sacrificed by cutting them off.

Once the foil is separated, it should stay on top of the water surface. It must be prevented that the foil floats to the edges of the container, because there is a possibility that it can stick to those edges. The movement of the floating foil can be manipulated by paddling the water near the foil with tweezers. Once the foil is in the middle of the container, it can be caught by a molybdenum grid ring.



Figure 60: A photograph of a 50 nm thick tungsten dummy foil that is being caught from the water by a molybdenum grid ring.

This process is reversible, so the foil can be removed from the molybdenum grid if it is slowly slid into the water.

C High temperature oven controller

A controller was developed to simplify the annealing process. It functions as a closed loop PID controller, a temperature display and a data logger. The controller is operated by a single rotary encoder knob and button combination. The front of the device is shown in Figure 61.

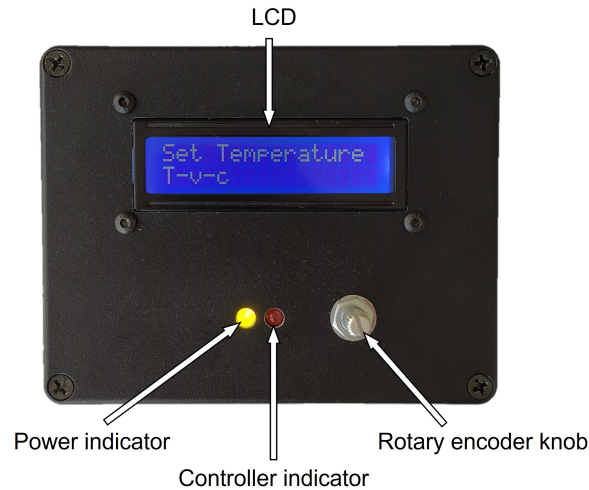


Figure 61: A photograph which shows the front panel of the oven controller.

An Arduino Nano board with an ATmega328P microcontroller runs the PID controller. It is connected with a TWI (Two-Wire Interface) bus to an ADC (Analog to Digital Converter), a DAC (Digital to Analog Converter) and an LCD (Liquid-Crystal Display). The input signal from the C type thermocouple passes a LC-filter and is then amplified by a differential amplifier using a TL072 clone. The amplified signal is measured by the ADS1115 ADC. The power supply of the oven is controlled with a 0 to 5 V signal that is generated by MCP4725 DAC. All electronic components within their aluminum enclosure are shown in Figure 62.

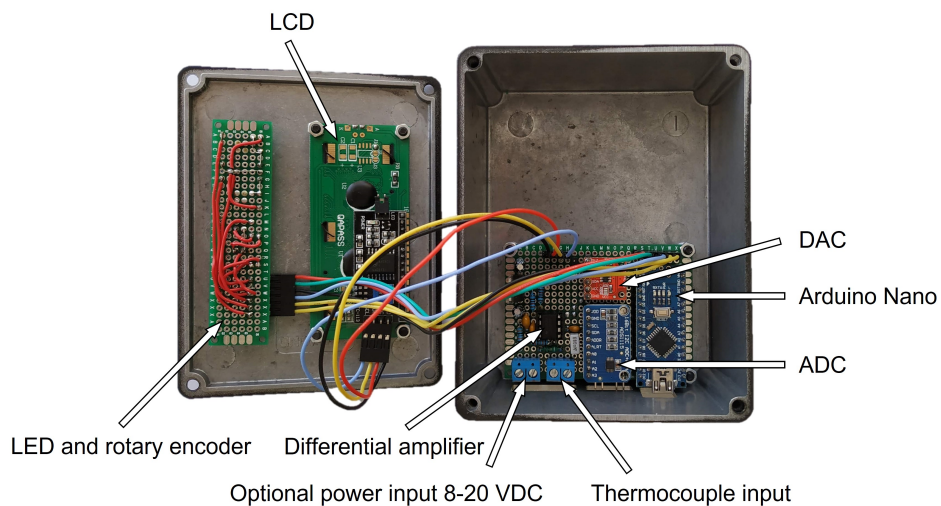


Figure 62: A photograph which shows the inside of the oven controller.

The temperature controller has all its connectors on one side. The device can be powered with a DC voltage between 8 and 20 V using an internal voltage regulator. It can also be powered over USB. Jumpers below the ADC board must be switched to select between the voltage regulator or USB power. The thermocouple can be connected to a screw terminal or pin headers. The voltage output for power

supply of the oven can only be connected with pin headers. A photograph of the input and output connectors of the temperature controller is shown in Figure 63.

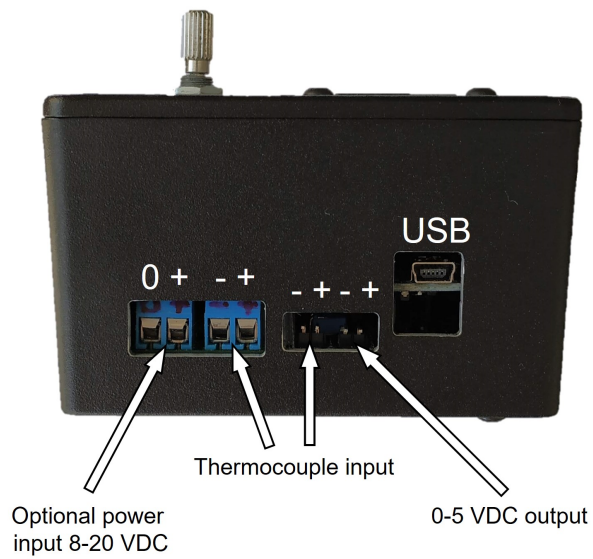


Figure 63: A photograph which shows the input and output of the oven controller.

The temperature controller uses a virtual serial connection over USB to send the elapsed time in s, the thermocouple temperature in °C and the thermocouple voltage in mV. The baud rate for this serial connection is 9600.

D Full drawing of the VEP facility

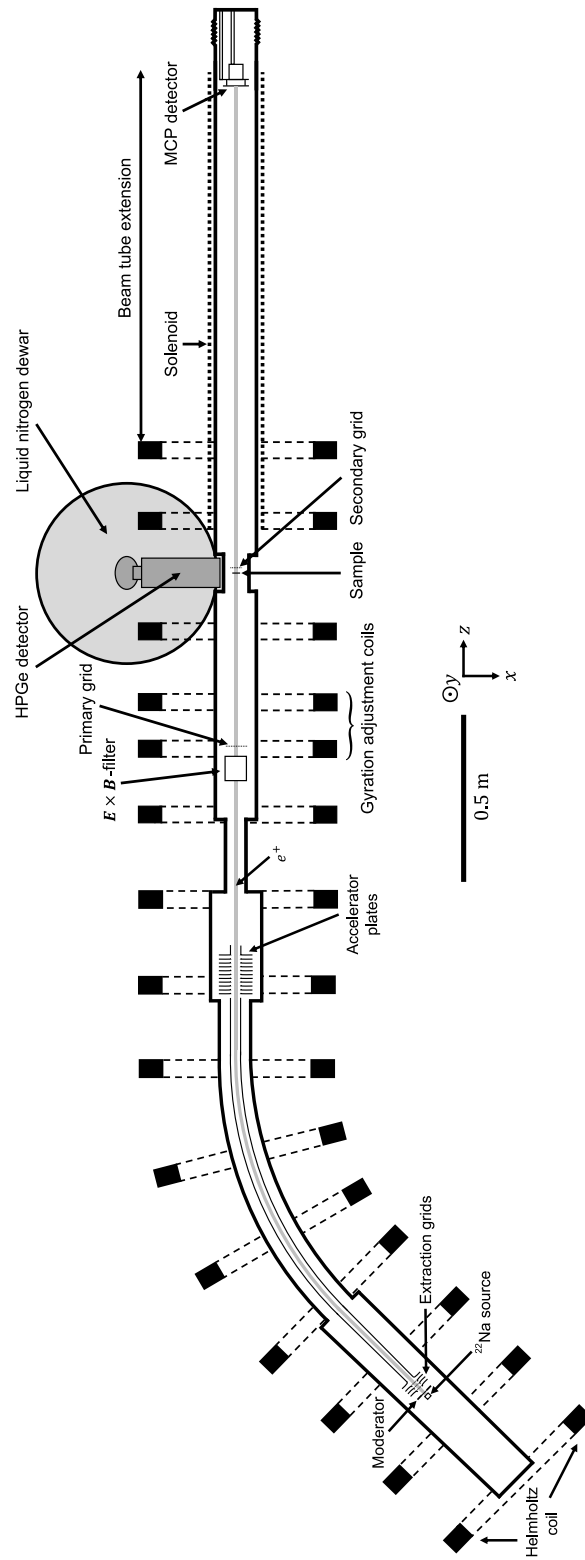


Figure 64: A sectional drawing of the VEP facility with modifications.

E Python code for moderator simulation

This script was used to generate figures 39, 40 and 41.

```
1 import numpy as np
2 import matplotlib.pyplot as plt
3
4 fileName = 'tfm_simulation'
5
6 #Simulation configuration
7 dz = 0.1 #nm (Step size)
8 E_min = 0.01 #keV (Minimum positron energy)
9 E_max = 25.0 #keV (Maximum positron energy)
10 dE = 0.05 #keV (Energy stepsize)
11
12 #Material properties and sample configuration
13 L = 50.0 #nm (Foil thickness)
14 rho = 1.925*10**(-14) #ug/(nm^3) (Material mass density)
15 L_plus = 50.0 #nm (Diffusion length)
16 lambda_b = 1*10**10 #1/s (Bulk annihilation rate)
17 nu_t = 10**(15) #1/s (Specific positron trapping rate for defects)
18 n_t = 3*10**(-5) #- (Defect concentration)
19 S_b = 0.49 #- (S-parameter bulk)
20 S_t = 0.49 #- (S-parameter defect)
21 S_s = 0.50 #- (S-parameter surface)
22
23 #Surface properties
24 epsilon_ps_F = 0.33 #- (Front surface positronium fraction)
25 epsilon_eplus_F = 0.33 #- (Front surface reemitted positron fraction)
26 epsilon_ss_F = 0.34 #- (Front surface bound positron fraction)
27
28 epsilon_ps_R = 0.33 #- (Rear surface positronium fraction)
29 epsilon_eplus_R = 0.33 #- (Rear surface reemitted positron fraction)
30 epsilon_ss_R = 0.34 #- (Rear surface bound positron fraction)
31
32 l_epi = 0.1 #nm (Epithermal scattering length)
33
34 #Makhov parameter
35 N_makhov = 4.51*10**(-14) #ug/(nm^2 keV^n_makhov)
36
37 #Variable precalculation
38 net_annihilation_rate = nu_t*n_t + lambda_b
39 distribution_parameter = N_makhov/rho
40 D_plus = net_annihilation_rate*L_plus**2 #nm^2/s (Positron diffusion coefficient)
41 kappa_t = nu_t*n_t #1/s (Positron trapping rate into defects)
42 S_prime = (lambda_b*S_b + kappa_t*S_t)/(lambda_b+kappa_t)
43
44 def greens_function(z, z0, net_annihilation_rate, D_plus, L):
45     annihilation_diffusion_coefficient = np.sqrt(net_annihilation_rate/D_plus)
46     return np.select([z < z0, z >= z0], [-np.sinh(annihilation_diffusion_coefficient*(z0-L))
47     *np.sinh(annihilation_diffusion_coefficient*z), -np.sinh(
48     annihilation_diffusion_coefficient*(z-L))*np.sinh(
49     annihilation_diffusion_coefficient*z0)])/(np.sinh(
50     annihilation_diffusion_coefficient*L)*annihilation_diffusion_coefficient*D_plus)
51
52 #Generating arrays
53 z = np.arange(0, L, dz)
54 z_matrix = np.array([z,]*len(z))
55 E = np.arange(E_min, E_max, dE)
56 c = np.zeros((len(z), len(E)))
57 F_implanted = np.zeros_like(E)
58 F_thermalized = np.zeros_like(E)
59 F_epi_0 = np.zeros_like(E)
60 F_epi_L = np.zeros_like(E)
61
62 #Calculate Epithermal positron probability curves
63 fd_epi_0 = np.exp(-z/l_epi)
64 fd_epi_L = np.exp((z-L)/l_epi)
65
66 z0 = distribution_parameter*E**1.62
```

```

64 #Integrate and sum
65 for energy in range(len(E)):
66     P = np.exp(-(z/z0[energy])**2)*2*z/(z0[energy]**2) #Calculating Makhov distribution
67     P_epi_0 = fd_epi_0*P #Epithermal positron fraction front
68     P_epi_L = fd_epi_L*P #Epithermal positron fraction rear
69     P_implanted = P - P_epi_0 - P_epi_L #Implantation profile
70     F_implanted[energy] = np.trapz(P_implanted, z) #Implanted positron fraction
71     F_epi_0[energy] = np.trapz(P_epi_0, z) #Epithermal positron fraction front
72     F_epi_L[energy] = np.trapz(P_epi_L, z) #Epithermal positron fraction rear
73     g = greens-function(z-matrix, np.transpose(z-matrix), net-annihilation-rate, D-plus,
74         L)
75     c[:, energy] = np.matmul(g, P_implanted*dz)
76     F_thermalized[energy] = np.trapz(c[:, energy], z) #Calculating the thermalized
77         positron fraction
78
79 F_fs = D-plus*np.gradient(c, z, axis=0)[0, :] #Fraction of positrons that reach the front
80     surface diffusion
81 F_rs = -D-plus*np.gradient(c, z, axis=0)[-1, :] #Fraction of positrons that reach the rear
82     surface diffusion
83
84 #Fractions front surface
85 F_fps = F_fs*epsilon-ps-F #Positronium fraction front
86 F_fps_ortho = F_fps*0.75 #Ortho-positronium fraction front (3-gamma annihilation)
87 F_fps_para = F_fps*0.25 #Para-positronium fraction front
88
89 F_feplus = F_fs*epsilon-eplus-F #Positron emission fraction
90 F_fss = F_fs*epsilon-ss-F #Surface bound positrons fraction
91
92 #Fractions rear surface
93 F_rps = F_rs*epsilon-ps-R #Positronium fraction
94 F_rps_ortho = F_rps*0.75 #Ortho-positronium fraction rear (3-gamma annihilation)
95 F_rps_para = F_rps*0.25 #Para-positronium fraction rear
96
97 F_replus = F_rs*epsilon-eplus-R #Positron emission fraction
98 F_rss = F_rs*epsilon-ss-R #Surface bound positron fraction
99
100 F_a = net-annihilation-rate*F_thermalized #Fraction of annihilated positrons in bulk and
101     defects
102 F_s = F_fss+F_rss + F_fps_para + F_rps_para #Fraction of annihilation near surface
103 F_Pk_sample = F_a + F_s #Detected fraction annihilation detector
104 S_parameter = F_s*S_s/F_Pk_sample + F_a*S_prime/F_Pk_sample #S parameter
105 F_Pk_sample_pos-grid = F_Pk_sample + F_feplus #Detected fraction annihilation detector
106     with positively charged primary grid
107 F_Pk_transmission = np.exp(-(L/z0)**2) + F_replus + F_epi_L #Detected fraction
108     transmission detector
109 F_Pk_transmission_pos-grid = np.exp(-(L/z0)**2) + F_epi_L #Detected fraction
110     transmission detector with positively charged secondary grid
111
112 optimal_implant_energy_index = np.argmax(F_replus)
113 plt.figure()
114 plt.plot(E, F_feplus, label=r'Front_surface_emission', c='k', linestyle='—')
115 plt.plot(E, F_replus, label=r'Rear_surface_emission', c='k')
116 plt.scatter(E[optimal_implant_energy_index], F_replus[optimal_implant_energy_index],
117     marker='o', facecolors='white', edgecolors='k', label=(f'Maximum,  $E_{opt}$  + str
118     (round(E[optimal_implant_energy_index], 1)) + '_keV,  $\eta_{opt}$  + str(round(100*
119     F_replus[optimal_implant_energy_index])) + '%'), zorder=5)
120 plt.legend()
121 plt.ylabel(r'$F_{e^+}$')
122 plt.xlabel(r'$E_{e^+}$ (keV)')
123 if(True):
124     plt.savefig(fileName + '_Ffe-Fre' + '.pdf')
125 plt.show()
126 plt.close()
127
128 fig, ax = plt.subplots()
129 ax.plot(E, S_parameter, label=r'$S(E)$', c='k')
130 ax.set_ylabel(r'$S$')
131 ax.set_xlabel(r'$E_{e^+}$ (keV)')
132 ax.axhline(y=S_prime, color='k', linestyle=':', label=r'$S'$")

```

```

122 ax.axhline(y=S_s, color='k', linestyle=':', label=r'S_s')
123 ax.set_yticks([S_s, S_prime])
124 ax.set_yticklabels([r'$S_s$', r'$S'$])
125 if(False):
126     ax.savefig(fileName + '_S' + '.pdf')

128 plt.figure()
129 plt.plot(E, F_Pk_sample, label=r'$G_{1\omega}$', c='k', linestyle='—')
130 plt.plot(E, F_Pk_sample_pos_grid, label=r'$G_{1\omega+}$', c='k')
131 plt.legend()
132 plt.ylabel(r'$R_A/R_{\omega}(-)$')
133 plt.xlabel(r'$E_{\omega}(\text{keV})$')
134 if(True):
135     plt.savefig(fileName + '_Pk_A_pm' + '.pdf')
136 plt.show()
137 plt.close()

139 plt.figure()
140 plt.plot(E, F_Pk_transmission_pos_grid, label=r'$G_{2\omega+}$', c='k')
141 plt.plot(E, F_Pk_transmission, label=r'$G_{2\omega}$', c='k', linestyle='—')
142 plt.legend()
143 plt.ylabel(r'$R_T/R_{\omega}(-)$')
144 plt.xlabel(r'$E_{\omega}(\text{keV})$')
145 if(True):
146     plt.savefig(fileName + '_Pk_T_pm' + '.pdf')
147 plt.show()
148 plt.close()

```